






Recent advances in CO₂ capture and reduction

Cite this: *Nanoscale*, 2022, **14**, 11869 Kecheng Wei, ^a Huanqin Guan, ^a Qiang Luo, ^b Jie He ^{*b,c} and Shouheng Sun ^{*a}

Given the continuous and excessive CO₂ emission into the atmosphere from anthropomorphic activities, there is now a growing demand for negative carbon emission technologies, which requires efficient capture and conversion of CO₂ to value-added chemicals. This review highlights recent advances in CO₂ capture and conversion chemistry and processes. It first summarizes various adsorbent materials that have been developed for CO₂ capture, including hydroxide-, amine-, and metal organic framework-based adsorbents. It then reviews recent efforts devoted to two types of CO₂ conversion reaction: thermochemical CO₂ hydrogenation and electrochemical CO₂ reduction. While thermal hydrogenation reactions are often accomplished in the presence of H₂, electrochemical reactions are realized by direct use of electricity that can be renewably generated from solar and wind power. The key to the success of these reactions is to develop efficient catalysts and to rationally engineer the catalyst–electrolyte interfaces. The review further covers recent studies in integrating CO₂ capture and conversion processes so that energy efficiency for the overall CO₂ capture and conversion can be optimized. Lastly, the review briefs some new approaches and future directions of coupling direct air capture and CO₂ conversion technologies as solutions to negative carbon emission and energy sustainability.

Received 25th May 2022,

Accepted 16th July 2022

DOI: 10.1039/d2nr02894h

rsc.li/nanoscale

1. Carbon cycle and CO₂ emission

Carbon is the chemical backbone of life on Earth. Carbon compounds regulate the Earth's temperature, make up the food that sustains us, and provide the energy that drives the global economy. The carbon cycle in nature is the global flow of carbon through the atmosphere, oceans, terrestrial biosphere, and lithosphere in various forms, such as carbon dioxide, organisms, limestone, coal and oil, as shown in Fig. 1A.¹ Two main cycles are the land–atmosphere cycle and the ocean–atmosphere cycle.^{2,3} The land–atmosphere cycle occurs through two main drivers: photosynthesis and respiration. In the photosynthesis process, CO₂ is absorbed from the

atmosphere and converted into fuels by plants or microbes, while in the respiration process CO₂ is produced as the final product from biological activities. In comparison with the land–atmosphere cycle, the ocean–atmosphere cycle plays a vital role in carbon storage because the ocean contains 50 times more carbon than the atmosphere.^{4,5} The driving mechanism of the ocean–atmosphere cycle is the difference in the partial pressure of CO₂ between the ocean and the atmosphere. This pressure varies with ocean temperature and local marine photosynthesis. The lower the ocean temperature, the smaller the carbon emissions.⁶ In all, nature balances these cycles well in equilibrium, maintaining the healthy evolution of life. Over the past century, however, fossil fuels have been massively consumed for energy uses (Fig. 1B).^{7,8} This has resulted in a dramatic increase in atmospheric CO₂, and as a result, caused a series of environmental issues, including global warming, acid rain, ocean acidification and rising sea levels (Fig. 1C).^{7–10}

^aDepartment of Chemistry, Brown University, Providence, Rhode Island 02912, USA. E-mail: ssun@brown.edu

^bDepartment of Chemistry, University of Connecticut, Storrs, Connecticut 06269, USA

^cPolymer Program, Institute of Materials Science, University of Connecticut, Storrs, Connecticut 06269, USA. E-mail: jie.he@uconn.edu

Kecheng Wei received his B.S. degree (2017) in Chemistry from the University of Science and Technology, China. He joined Prof. Shouheng Sun's group in 2017 and is currently a Ph.D. candidate in the Chemistry Department of Brown University. His research is in the shape-controlled synthesis of nanocatalysts for fuel cell reactions and CO₂ reduction.

Huanqin Guan obtained his B.S. degree from Peking University in 2018. He then joined Prof. Shouheng Sun's group and is currently a Ph.D. candidate in the Chemistry Department at Brown University. His research interests involve nanocatalyst synthesis and their applications in green chemistry reactions, and CO₂ capture and conversion.

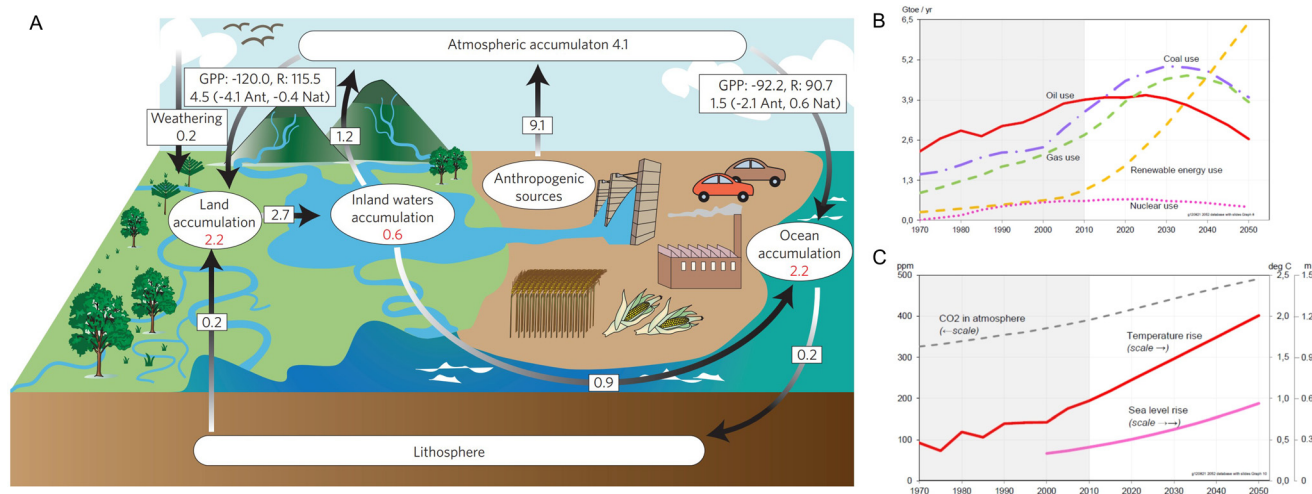


Fig. 1 (A) The schematic highlights carbon fluxes through inland waters and includes pre-industrial and anthropogenic fluxes. Values are net fluxes between pools (black) or rates of change within pools (red); units are Pg C per year; negative signs indicate a sink from the atmosphere. Gross fluxes from the atmosphere to land and oceans, and the natural (Nat) and anthropogenic (Ant) components of net primary production—the net uptake of carbon by photosynthetic organisms—are shown for land and oceans. Gross primary production (GPP) and ecosystem respiration (R). (B) Energy source in the past and forecast from 1970 to 2050, and (C) CO₂ concentration in atmosphere, global temperature, sea level. Adapted from ref. 1 and 9 with permission. Copyright 2009 Nature Publishing Group and 2012 Chelsea Green Publishing.

2. CO₂ capture

To combat anthropogenic CO₂ emission and to make our lifestyles sustainable, we must develop neutral or even negative carbon emission technologies. One such technology is CO₂ capture and storage.^{11,12} Recent studies have shown that the key barrier that limits the broad use of this process is the high energy penalty associated with CO₂ capture,¹² which is aggravated by the fact that about half of the annual CO₂ emission is generated from widespread industrial sites. In 1999, Lackner introduced the concept of direct air capture of CO₂ to mitigate climate change, and it is now broadly defined as direct extraction of CO₂ from ambient air.^{13–16}

A key step to successful CO₂ capture is to develop efficient adsorbents to bind CO₂ from air. An ideal CO₂ adsorbent should have high selectivity and adsorption capacity for CO₂, low heat of adsorption (Q_{st}), high recyclability, good thermal and chemical stability, fast kinetics and high cost-effectiveness

(Fig. 2).¹⁷ The energetics of the CO₂ capture process is about the chemical bonding nature between CO₂ and an adsorbent, which can involve both weak physisorption and strong chemisorption. Such binding strength is defined by the isosteric heat of adsorption Q_{st} (kJ mol⁻¹). For a given adsorbent, a high Q_{st} value indicates an energy-intensive CO₂ regeneration process once it is captured, whereas a low Q_{st} value may compromise the CO₂ adsorption capacity. Furthermore, a good adsorbent should have high selectivity for adsorbing CO₂ from a mixture of gases, especially from air, and have high thermal, chemical, and water stability to achieve high CO₂ capture efficiency under different operational conditions. The rate of CO₂ uptake should also be kinetically fast, the capture process should be easily engineered to large scale, and the overall cost for the capture process should be economically practical. Here we summarize some representative adsorbents that have been studied extensively for CO₂ capture, including aqueous hydroxide, solid alkali carbonates, organic amines, and porous materials.^{18,19}

Qiang Luo received his B.S. degree in Material Science and Engineering from Shaanxi Normal University in 2019. Currently, he is a Ph.D. student at the Department of Chemistry at the University of Connecticut under the supervision of Prof. Jie He. His research interests include the synthesis and applications of mesoporous materials and CO₂ reduction.

Jie He earned his B.S. and M.S. degrees in Polymer Materials Science and Engineering from Sichuan University and his Ph.D. in Chemistry from the Université de Sherbrooke in 2010. After working with Professor Zhihong Nie as a postdoctoral fellow at the University of Maryland, he joined the faculty of the University of Connecticut where he is currently an Associate Professor of Chemistry. His group focuses on the design of hybrid materials of polymers and inorganic materials (metal ions, clusters, and nanoparticles) being capable of catalyzing the activation of H₂O, O₂ and CO₂ as inspired by nature.

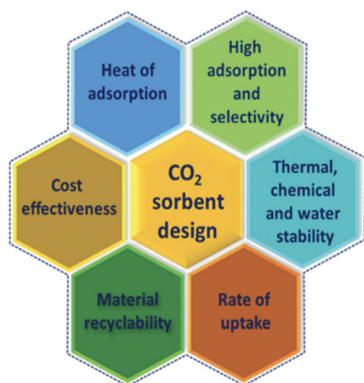


Fig. 2 Principal criteria for designing an ideal sorbent for CO₂ capture. Reprinted from ref. 17 with permission. Copyright 2020 Royal Society of Chemistry.

2.1. Hydroxide-based adsorbents

Due to the relatively low concentration of CO₂ (412 ppm) in the atmosphere, CO₂ capture is usually carried out using chemical adsorbents with a strong CO₂ binding affinity. A common adsorbent is calcium hydroxide solution, which can react with CO₂ and form calcium carbonate as precipitate. The calcium carbonate can then be separated and dried for storage. The captured CO₂ can be accessed through a process known as calcination – the decomposition of calcium carbonate to form calcium oxide with CO₂ being released as a concentrated stream. Calcium hydroxide is then regenerated in a slaking process *via* hydration of calcium oxide, forming a recyclable loop.¹⁴ Many different types of adsorption devices, from traditional stagnant pools, packed towers to modern spray towers, have been designed and developed.²⁰ Alternatively, solid inorganic bases are used for ultra-dilute CO₂ removal. Fig. 3 plots the equilibrium partial pressure of CO₂, $p_{\text{CO}_2, \text{eq}}$, as a function of temperature (T), for various single-metal oxide sorbents. Combinations of T and p_{CO_2} above the respective $p_{\text{CO}_2, \text{eq}}$ curves imply the material exists as carbonate, whereas below the curve, the material's thermodynamically stable state

Shouheng Sun received his Ph.D. in Chemistry from Brown University in 1996. He joined the IBM T. J. Watson Research Center (Yorktown Heights, New York) first as a postdoctoral fellow (1996–1998) and then as a research staff member (1998–2004). In 2005, he returned to Brown University as a tenured Associate Professor and was promoted to full Professor in 2007. He is now the Vernon K. Kriple Professor of Chemistry and Professor of Engineering. He served as Associate Editor of the Royal Society of Chemistry journals Nanoscale/Nanoscale Advances (2012–2021) and is a Fellow of the Royal Society of Chemistry. His main research interests are in chemical synthesis and self-assembly of nanoparticles for catalytic, magnetic, and biomedical applications.

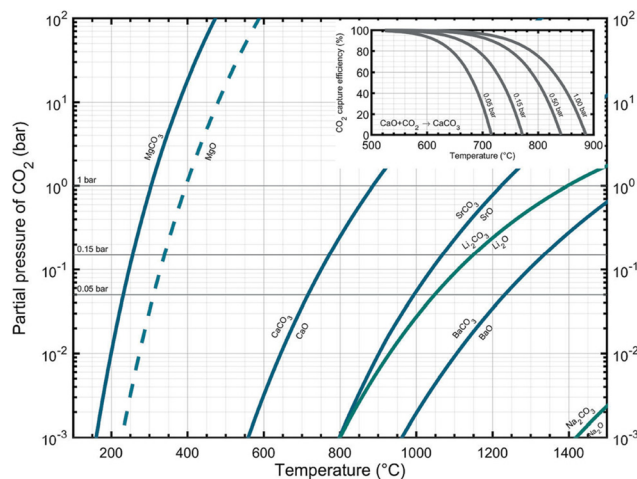


Fig. 3 Equilibrium partial pressure of CO₂, $p_{\text{CO}_2, \text{eq}}$, as a function of temperature for alkali (green) and alkaline earth (blue) metal oxide–carbonate systems. Horizontal gray lines indicate p_{CO_2} of 0.05, 0.15, and 1 bar, respectively. Reprinted from ref. 21 with permission. Copyright 2008 and 2021 American Chemical Society.

is its oxide form.²¹ The thermodynamic properties of the CaO–CaCO₃ system enable the direct capture of CO₂ from ambient air ($p_{\text{CO}_2} = 4 \times 10^{-4}$ bar). To release CO₂ from CaCO₃, high temperatures (>900 °C) are generally required to obtain a pure stream of CO₂ ($p_{\text{CO}_2} \approx 1$ bar). Despite the convenient chemistry involved in the process, dealing with a large volume of air, hydroxide solution, and metal carbonate decomposition can impose heavy energy cost due to the high temperature required to regenerate the metal oxide adsorbents and to release CO₂.

2.2. Amine-based adsorbents

Amines are another common adsorbent employed for CO₂ capture. Using aqueous solutions of amines to capture CO₂ has been extended to commercial uses to remove CO₂ from CO₂-rich natural gas streams.²² To date, amine adsorbents employed for direct air capture have been supported on solids to improve amine stability and recyclability. The strength of chemisorption between an amine and CO₂ ensures selective CO₂ uptake even at low CO₂ partial pressures, which makes the solid-supported amine adsorbents highly suitable for the direct air capture of CO₂.

In a dry condition, CO₂ reacts with either a primary amine (eqn (1)) or secondary amine (eqn (2)) to produce an ammonium carbamate. When moisture is present, the reaction yields ammonium carbonate or bicarbonate (depending on the pH) (eqn (3) and (4)).¹⁴ Amine-containing sorbents have been divided into three classes: class 1 amine adsorbents are prepared by impregnating amines into the pores of a support; class 2 amine adsorbents are formed by covalently bonding amines to the walls of porous materials *via* silane linkage; and class 3 amine adsorbents are derived from polymerization of amines *in situ* to form polyamine structures tethered to the inner walls of the porous support.^{14,23–25} Fig. 4 shows some representative examples of these amine adsorbents. After

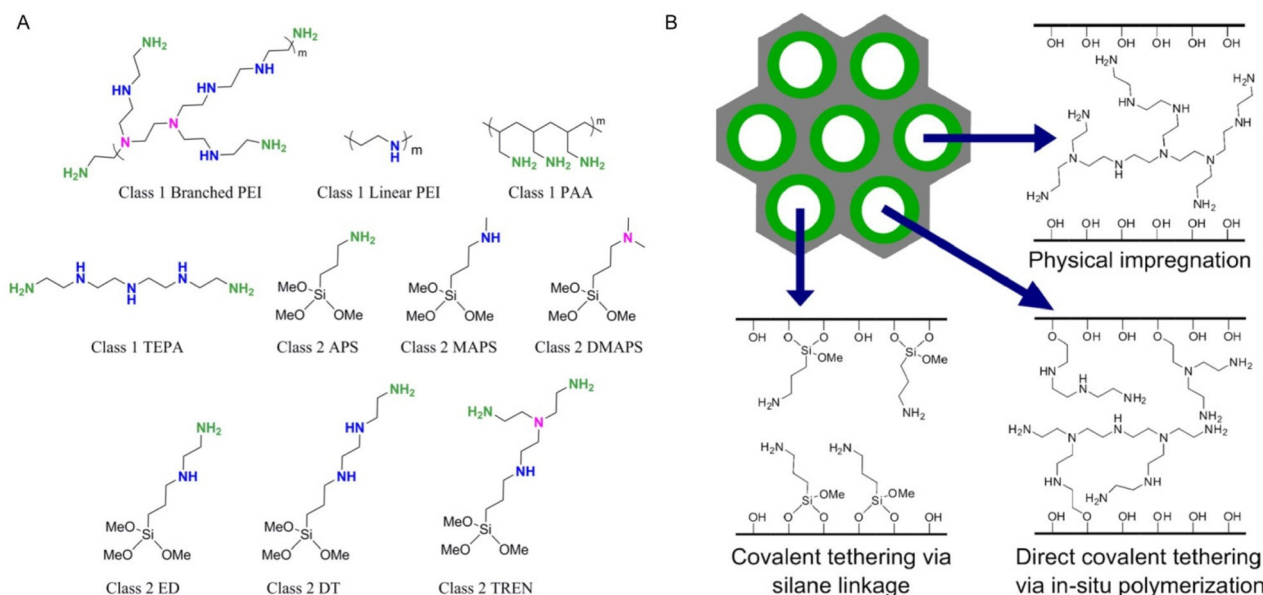
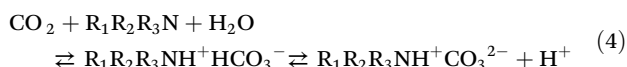
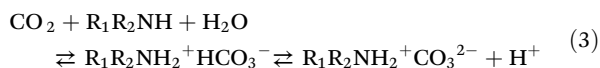
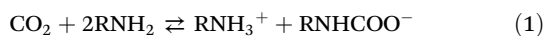


Fig. 4 (A) Molecular structures of commonly used amines for class 1 and class 2 direct air capture sorbents. (B) Schematic representation of the three main routes used for functionalization of porous supports with amine moieties. Reprinted from ref. 14 and 26 with permission. Copyright 2016 American Chemical Society and 2016 Georgia Institute of Technology.

adsorption, CO₂ can be released from the adsorbent by an inert gas flow to drive the reaction equilibrium towards gaseous CO₂.^{14,26} An advantage of the amine adsorbent over the metal oxide one is its selective adsorption of CO₂ over H₂O, making it useful in the humid environment.²⁷



2.3. Adsorbents based on metal organic frameworks (MOFs)

The cleavage of adsorbed CO₂ in the formation of carbonate and carbamate is endothermic; and it requires a large energy input to regenerate in case of a strong adsorbent. Weak physisorption of CO₂ by porous materials has been explored extensively as an alternative to chemisorption to improve the energy efficiency of the capture process. Significant research progress has been made in CO₂ capture by micro and mesoporous materials, including metal-organic frameworks (MOFs), zeolites, zeolitic imidazole frameworks (ZIF), and porous polymers.^{13,17,28,29} MOFs consist of three-dimensional coordination polymer networks, constructed by the combination of metal ions/clusters with organic linkers/ligands. Fig. 5 shows crystalline structures of some well-known MOFs.³⁰ Their CO₂ adsorption power can be tuned more conveniently by specific

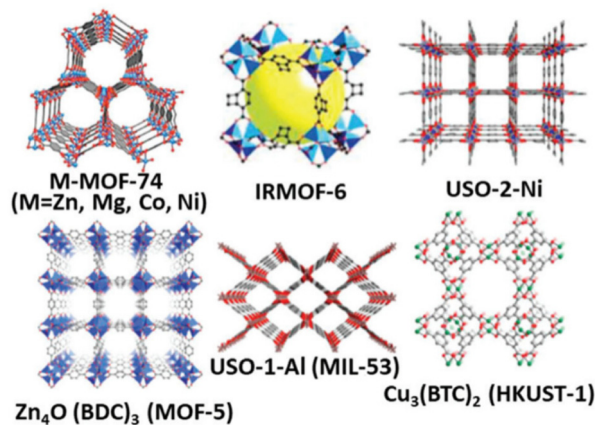


Fig. 5 Crystalline structures of some well-known MOFs. Reprinted from ref. 30 with permission. Copyright 2019 Elsevier.

surface areas, pore volumes, pore sizes, metal centres, and surface functional groups, which make them especially attractive for selective CO₂ capture from a stream of gas mixture.

2.3.1. CO₂ adsorption via metal-binding in MOFs. As the pore structures of MOFs are sensitive to the adsorption of CO₂, functionalization of the inner and outer surface of the MOFs can tune their adsorption power. A typical approach is to make MOFs with unsaturated open metal sites (UOMSSs), which can be prepared by heating or vacuuming of the solvent-coordinated metal cations in MOFs.^{30,31} These exposed metal-coordination sites can build an electric field around them, providing the desired driving force for CO₂ adsorption. M-CO₂ binding is realized by direct interaction between the antibond-

ing d^2 orbital and the lone electron pairs on the oxygen in the CO_2 molecule. For an early transition metal cation with d electrons less than 4, its antibonding d -orbitals tend to bind to CO_2 more strongly. But for a late transition metal cation, its antibonding orbitals can be filled up, weakening its binding with CO_2 .³² For example, $\text{Mg}_2(\text{dobdc})$ ($\text{H}_4\text{dobdc} = 2,5$ -dihydroxyterephthalic acid), Mg-MOF-74 , and CPO-27-Mg structures with open metal sites bind to CO_2 at a fixed angle in a uniaxial fashion, as shown in Fig. 6A.³³ Their CO_2 binding energies are around 67.2 kJ mol^{-1} (Fig. 6B).³⁴ In the presence of the early transition metal (Ti or V) cation, their binding energies increase to 73.2 – 80.2 kJ mol^{-1} , while in the presence of the late transition metal (Cr or Zn) cation, their binding energies drop to 32.2 – 50.8 kJ mol^{-1} (Fig. 6B).

2.3.2. Enhancing CO_2 adsorption via functionalization of MOFs. MOFs modified with functional groups can change their surface properties and CO_2 adsorption power. A common strategy to modify MOFs is to add polar or amine-based moieties to the structure to enhance their interactions with CO_2 , especially under low-pressure conditions. However, this enhancement needs to be regulated very carefully as the strong interaction with CO_2 also makes it difficult to regenerate the MOF adsorbent. Therefore, this functionalization should enable MOFs to show high CO_2 adsorption affinity, capacity, and selectivity, but low Q_{st} .

As an example, isorecticular MOF (IRMOFs)-74-III was functionalized with a series of organic linkers $-\text{CH}_3$, $-\text{NH}_2$, $-\text{CH}_2\text{NHBoc}$ (Boc: *tert*-butyloxycarbonyl), $-\text{CH}_2\text{NMeBoc}$, $-\text{CH}_2\text{NH}_2$, and $-\text{CH}_2\text{NHMe}$ via the Suzuki–Miyaura coupling reaction (Fig. 7A).^{35,36} All the modified MOFs, except the ones containing the protective Boc groups, showed high and similar CO_2 adsorption behaviours at $25 \text{ }^\circ\text{C}/800 \text{ Torr}$, as shown in Fig. 7B.³⁶ However, at low pressure, primary amine- and secondary amine-functionalized MOFs (IRMOF-74-III- CH_2NH_2 and IRMOF-74-III- CH_2NHMe , respectively) outperformed the other modified MOFs (Fig. 7C).³⁶ A second CO_2 isotherm after evacuation of the sample at room temperature for 2 h and a third cycle with a heat treatment at $120 \text{ }^\circ\text{C}$ under vacuum (10 mTorr) for 1 h was recorded (Fig. 7D and E).³⁶ The decrease in CO_2 uptake on the second cycle and recovery upon heat

treatment indicated the presence of strongly bound CO_2 . Further exploration of IRMOF-74-III- CH_2NH_2 using dynamic CO_2 adsorption under dry ($16\% \text{ CO}_2$; $84\% \text{ dry N}_2$) and wet ($16\% \text{ CO}_2$; $84\% \text{ wet N}_2$) conditions showed a negligible difference in the uptake rates for the CO_2 adsorption, suggesting the unique structural selectivity towards CO_2 . ^{13}C NMR studies showed that the capture was realized by chemisorption between CO_2 and the functionalized organic linkers, forming carbamate ions and carbamic acids for IRMOF-74-III- CH_2NH_2 and IRMOF-74-III- CH_2NHMe , respectively. Incorporation of diamine groups into the same MOF to form IRMOF-74-III- $(\text{CH}_2\text{NH}_2)_2$ could provide an even higher CO_2 adsorption power at $25 \text{ }^\circ\text{C}/800 \text{ Torr}$ ($75 \text{ cm}^3 \text{ g}^{-1}$) than that of IRMOF-74-III- CH_2NH_2 ($67 \text{ cm}^3 \text{ g}^{-1}$).³⁷

2.3.3. MOF pore size-dependent CO_2 adsorption. The pore size is a third common parameter that can be applied to control MOF's CO_2 adsorption capability and selectivity. It is possible to synthesize MOFs with microporosity, mesopores or macropores, which can be controlled by the nature of metal precursors and organic linkers used during synthesis.^{38,39} For example, MOFs with pore size of 2.6, 2.4, and 2.2 nm could be synthesized using cobalt–organic linkers with slightly different configurations (IR-MOF-74-III).⁴⁰ The benzene rings were termed as pore size tuners and the CO_2 adsorption of the three MOFs was enhanced as the pore size decreased from 2.6 to 2.2 nm. The competing adsorption of water could be suppressed by narrowing down the pore size as suggested by computational calculations and experimental demonstration on MOF-74 by inserting 2,4,6-tri(4-pyridyl)-1,3,5-triazine (tpt) into its hexagonal channels.⁴¹

3. CO_2 reduction

Despite the fact that CO_2 capture is important to solve CO_2 emission problems, to realize energy sustainability, CO_2 must be converted back into chemical fuels, which requires the controlled reduction and protonation of CO_2 . This process is unfortunately energetically uphill due to the high activation energy needed to break the stable $\text{O}=\text{C}$ bonds and the apparent difference in free energy between CO_2 and the final products. For this reaction to be economically viable, suitable catalysts with high catalytic activity, selectivity and stability must first be developed to achieve energy-efficient reduction of CO_2 . Many chemistry processes, including thermochemistry, electrochemistry, photochemistry, and biochemistry processes, have been studied for CO_2 reduction. In this section we highlight the recent advances in thermo- and electro-catalytic reduction of CO_2 .

3.1. CO_2 activation

CO_2 is a very stable molecule, with a bond dissociation energy of $525.9 \text{ kJ mol}^{-1}$ and ionization potential of 13.777 eV , making CO_2 activation difficult and costly.⁴² One-electron reduction of CO_2 is believed to be the first step to initiate the reduction and other reaction processes that convert CO_2 to reu-

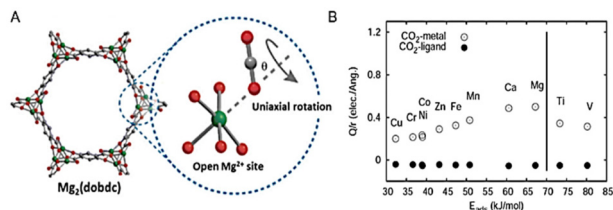


Fig. 6 (A) Schematic illustration of CO_2 uniaxial rotation at the open Mg^{2+} site in $\text{Mg}_2(\text{dobdc})$. Gray – C, red – O, and green – Mg atoms; H atoms are omitted for clarity. The blue circle is the arbitrary rotation axis. (B) CO_2 adsorption energy plotted over Q/r computed for the metal– CO_2 oxygen distance and the tetrazole nitrogen– CO_2 carbon distance. The vertical line is to guide the eye. Reprinted from ref. 33 and 34 with permission. Copyright 2012 and 2014 American Chemical Society.

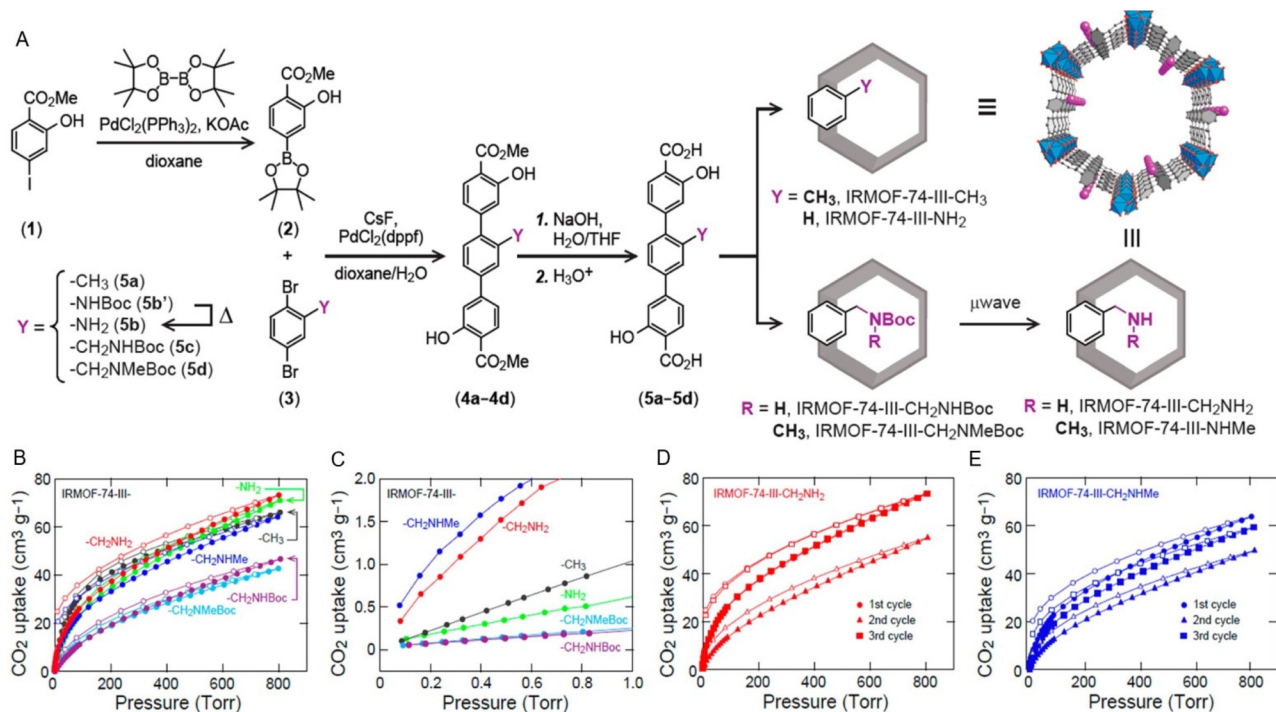


Fig. 7 (A) Synthetic pathway for the functionalized organic linkers used in the synthesis of IRMOF-74-III, in the preparation of $-\text{CH}_3$ (5a), $-\text{NH}_2$ (5b), $-\text{CH}_2\text{NHBoc}$ (5c), and $-\text{CH}_2\text{NMeBoc}$ (5d) functionalized linkers. On the right is shown a schematic representation of the IRMOF-74-III pore as functionalized with the organic linkers 5a–5d and post-synthetic deprotection of Boc groups. Color code: C in gray, O in red, functional groups in purple, Mg as blue polyhedra. (B) Comparison of CO_2 uptake at 25 °C for IRMOF-74-III- CH_3 (gray), $-\text{NH}_2$ (green), CH_2NH_2 (red), $-\text{CH}_2\text{NHMe}$ (blue), $-\text{CH}_2\text{NHBoc}$ (purple), and $-\text{CH}_2\text{NMeBoc}$ (cyan). (C) Expansion of the low-pressure range (>1 Torr). Carbon dioxide isotherms at 25 °C for IRMOF-74-III- CH_2NH_2 (D) and $-\text{CH}_2\text{NHMe}$ (E). Uptakes for samples after activation (first cycle), after first CO_2 uptake (second cycle), and after 120 °C heating for 1 h for regeneration (third cycle) are shown in circles, triangles, and squares, respectively. Reprinted from ref. 36 with permission. Copyright 2014 American Chemical Society.

sable forms of carbon. The electronic structure of CO_2 in different charge states can be summarized in its Walsh diagram (Fig. 8A).⁴³ In the ground state of neutral CO_2 , the highest occupied molecular orbital (HOMO) is the fully occupied $1\pi_g$ orbital. An excess electron will be accommodated in the $2\pi_u$ orbital, which is stabilized by bending the molecule, leading to a deviation of the molecular symmetry from $D_{\infty h}$ to C_{2v} . The singly occupied molecular orbital (SOMO) in this radical anion is of a_1 symmetry, with an OCO angle calculated to be 138°, and it can be described as pseudo-antibonding. At the same time, the bonding $1\pi_g$ orbital transforms into a_2 and b_2 orbitals that have been characterized as largely nonbonding.⁴⁴ Consistent with the pseudo antibonding nature of the HOMO of CO_2^- , its C–O bond length (124 pm) is greater than that of the neutral CO_2 (117 pm).

The free CO_2^- radical anion is metastable and has been observed in mass spectrometry with measured lifetime up to milliseconds.⁴⁴ The radical anion can be stabilized by interaction with a matrix or by solvation. The solvated CO_2^- radical anion has been observed in bulk solutions as well as in $(\text{CO}_2)_n^-$ ($n = 6\text{--}13$) cluster ions.⁴⁴ While the first electronic excited state of neutral CO_2 is in the deep ultraviolet (UV), the radical anion has its lowest excited state in the near UV range. The electronic absorption band of CO_2^- is at about 235 nm

and CO_2^- can dissociate upon excitation and lose its excess electron by charge transfer, making it challenging to fully characterize CO_2^- .

Understanding the binding between CO_2 and a metal surface is of great importance for developing a metal catalyst to catalyse CO_2 reduction reaction. CO_2 can bind to metal atoms *via* different binding motifs, as summarized in Fig. 8B.⁴⁴ These modes are abbreviated as $\eta^1\text{-C}$, $\eta^1\text{-O}$, $\eta^2\text{-C,O}$, and $\eta^2\text{-O,O}$, where superscripts denote the number of bonds

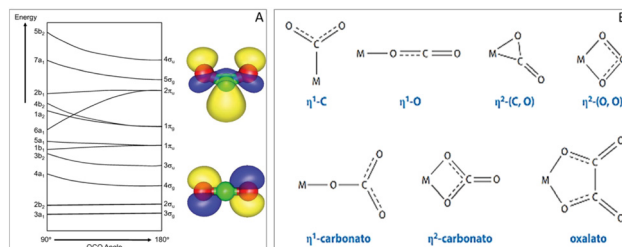


Fig. 8 (A) Walsh diagram of CO_2 , with illustrations of the highest occupied molecular orbitals of the anion (top) and the neutral (bottom). (B) Structural motifs of metal- CO_2 interactions. Reprinted from ref. 43 and 44 with permission. Copyright 2014 Abingdon: Taylor & Francis and 2018 Annual Reviews.

between the metal atoms and bound CO_2 , and the chemical element symbols describe the atoms directly interacting with the metal. Electron reduction of metal- CO_2 leads to the formation metal- CO_2 cluster anions, $[\text{M}(\text{CO}_2)_n]^-$ that can serve as simplified models for studying CO_2 binding to metal atoms present on catalyst surfaces.^{45–47}

3.2. Thermal reduction of CO_2

The reduction of CO_2 in a thermo-catalytic process has attracted much attention as it not only reduces CO_2 emission, but also directly produces value-added chemicals and fuels.⁴⁸ To transform CO_2 to downstream products, its thermodynamic reaction barrier must be overcome.⁴⁹ Using H_2 as a high-energy reactant to reduce CO_2 has been a common approach, as H_2 can be generated from water electrolysis by renewable (solar or wind) electricity.⁴⁸ Therefore, this conversion of CO_2 by catalytic thermo-hydrogenation is one of the most attractive approaches to sustainable energy and a carbon-neutral cycle (Fig. 9A).⁵⁰

3.2.1. Reversible water-gas shift (RWGS) reaction to CO. CO is considered as the most crucial intermediate in CO_2 conversion as it can be coupled in methanol synthesis and Fischer-Tropsch (FT) synthesis of various chemicals and fuels (Fig. 9B).⁵¹ CO is generally produced by the reversible water-gas shift (RWGS) reaction, in which CO_2 is hydrogenated under a high-temperature and high-pressure condition. However, this reaction quickly reaches its equilibrium, and as a result, the reaction has a low conversion yield (23%) at 300 °C and 1 MPa.⁵² Two mechanisms have been reported to

explain the CO_2 hydrogenation to CO. The first one is a redox mechanism, which is usually observed on the surface of Cu-based catalysts. CO_2 is reduced by Cu^0 to form CO^* , which is desorbed from the surface to form CO product, and Cu^+ is then reduced back to Cu^0 by H_2 with water being formed as a byproduct.⁵³ This is further supported by density functional theory (DFT) calculations and Fourier-transform infrared spectroscopy (FTIR) spectroscopy studies over a Cu/ZnO catalyst.⁵⁴ The CO_2 hydrogenation may also follow the formate pathway, in which CO_2 is first converted to formate that is further dehydrated to form CO.⁵⁵

Metals on oxide supports are considered as promising catalysts as the metal centres could easily dissociate H_2 , which is followed by transfer of H^* to CO_2 adsorbed on the oxide support.⁵⁶ Various catalysts based on transition metals on different oxide supports have been studied for the RWGS reaction. Among them, Cu or Pt-based catalysts supported on CeO_2 are the most extensively studied.⁵⁷ In studying monometallic and bimetallic Pt-based catalysts on different oxide supports for selective CO_2 conversion to CO, it was found that active metal controlled the product selectivity, while the support effect dominated the activity of CO_2 conversion.⁵⁸ For the monometallic Pt catalysts, a reducible support (CeO_2) showed higher activity than an irreducible support ($\gamma\text{-Al}_2\text{O}_3$) because of the increased oxygen vacancies found in the CeO_2 structure, which are beneficial for oxygen exchange with CO_2 . Among the bimetallic Pt-based catalysts supported on CeO_2 , PtCo showed the highest CO selectivity with little CH_4 production due to the weak binding of CO on the metal surface (Fig. 10A).⁵⁸ Based on the d band theory, the CO/ CH_4 ratio selectivity increases when the values of the d-band centre move towards more negative values for the Pt, Co, and Ni-based catalysts on either CeO_2 or $\gamma\text{-Al}_2\text{O}_3$ supports (Fig. 10B).⁵⁸ Such correlation between CO selectivity and metal d-band centre is potentially helpful for predicting selective CO_2 reduction catalysts.

In addition to Pt, other precious metals, such as Ir, Ru, Rh and Pd, are reported to be highly active hydrogenation catalysts.⁵⁹ Alternatively, Cu, Fe and Ni-based catalysts are also being explored for large-scale RWGS.⁶⁰ Cu/ CeO_2 was found to be especially active as a RWGS catalyst at low temperature (300 °C) and ambient pressure, reaching 100% CO selectivity.⁶¹ The enhanced activity was attributed to synergies of Cu nano-

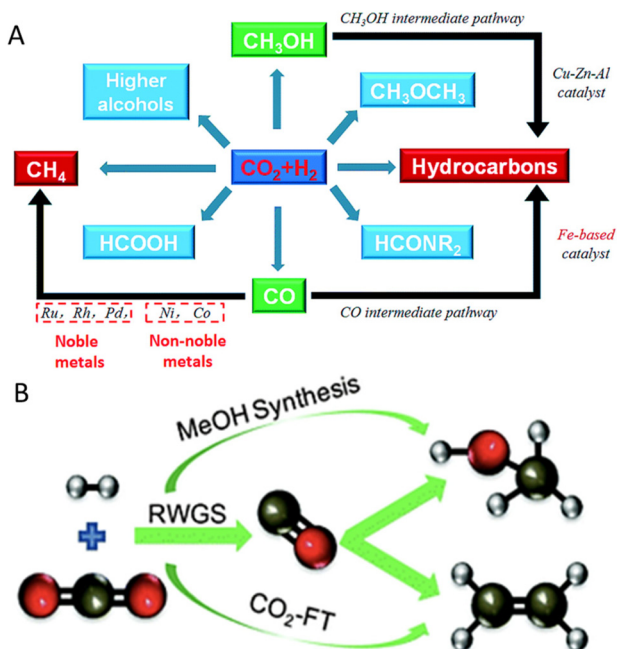


Fig. 9 (A) Conversion of CO_2 to chemicals and fuels through hydrogenation. (B) Schematic illustration of cycles between RWGS, CO_2 -FT and methanol synthesis. Reprinted from ref. 50 and 51 with permission. Copyright 2016, 2018 Royal Society of Chemistry.

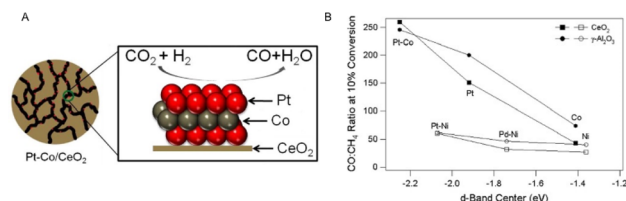


Fig. 10 (A) Pt-Co/ CeO_2 for CO_2 hydrogenation to CO. (B) Effect of d-band centre on ratio of CO to CH_4 production at 10% conversion. For ease of comparison, open and solid symbols represent catalysts with and without Ni, respectively. Reprinted from ref. 58 with permission. Copyright 2013 Elsevier.

particle (NP) and CeO_x support in their redox behaviours and oxygen vacancies (Fig. 11A).⁶¹ *In situ* Ce L₃-edge XANES measurement for CeO_2 and Cu– CeO_2 supported on mesoporous silica SBA-15 (denoted as S_{Ce} and S_{CuCe}, respectively) was performed during sample reduction at 300 °C in H_2 (Fig. 11B and C).⁶¹ No change was observed in S_{Ce} after reduction, while there was partial reduction of Ce^{4+} to Ce^{3+} for S_{CuCe}. Similarly, Cu structure change upon CO_2 treatment at 120 °C was detected by *in situ* X-ray absorption spectroscopy (XAS) measurement (Fig. 11D and E).⁶¹ The spectra corresponded well with the Cu_2O standard, suggesting that Cu^0 species in S_{CuCe}-re are oxidized to Cu^+ species *via* CO_2 treatment at 120 °C.⁶¹ The rapid desorption of CO from Cu^+ –CO intermediate at the reaction temperature led to product formation, which was followed by facile reduction of Cu and Ce by hydrogen spillover. The results suggest that the synergistic effect between oxygen vacancies and Cu redox property is essential for the oxide-supported Cu catalyst to show high RWGS activity and selectivity.

3.2.2. Thermal reduction of CO_2 to methanol. Methanol is an important chemical feedstock for uses in combustion engines, fuel cells, and in the synthesis of downstream value-added products, such as dimethyl ether and hydrocarbons.⁶² The so called “methanol economy” is an indispensable and promising component in the carbon capture and conversion process to achieve a carbon neutral cycle.⁶³ In fact, 140 million tons of methanol were produced in 2018 and its production is

expected to double by 2030.⁶⁴ Conventionally, methanol is produced from syngas ($\text{CO} + \text{H}_2$) over a $\text{Cu}/\text{ZnO}/\text{Al}_2\text{O}_3$ catalyst at 200–300 °C and 3.0–5.0 MPa, but further studies indicate that CO_2 -blended syngas shows higher reaction rates than syngas alone under the same reaction conditions.^{62,65} As a result, direct hydrogenation of CO_2 to methanol has been a hot trend of research. Oxide-supported Cu catalysts are popular choices for methanol synthesis from CO_2 . In the Cu/ZnO catalyst system, the high catalytic activity is attributed to the special Cu/ZnO interfacial and CuZn surface alloy effects, as confirmed by studying $\text{CuZn}(111)$ and $\text{ZnO}/\text{Cu}(111)$ catalysis.⁶⁶ In this study, CuZn was found to undergo surface oxidation under reaction conditions and the surface Zn was transformed into ZnO. The catalysis showed a volcano-plot trend between methanol production and ZnO coverage on $\text{Cu}(111)$ (Fig. 12A and B).⁶⁶ Similarly, $\text{CuZn}(211)$ catalysis was further enhanced once the CuZn surface was partially covered with ZnO. The catalysis enhancement was attributed to the strong metal–support interaction, which strengthens the surface binding to intermediates and increases the catalytic activity.⁶⁷

Since CO_2 conversion to methanol is sensitive to catalyst structure, it is important to maintain the catalyst dispersion and prevent the catalyst from sintering and deactivation under the reaction conditions.⁶⁸ Various strategies have been proposed to solve the deactivation issues, including the use of reducible supports and encapsulation of Cu in metal organic frameworks (MOFs).^{69,70} For example, a Cu-MOF-based composite catalyst was prepared by encapsulating Cu within the Zr-based UiO-66 porous structure.⁷⁰ The stabilized Cu showed much higher activity toward methanol formation (Fig. 12C).⁷⁰ Additionally, the SiO_2 -supported Ni–Ga intermetallic catalyst was found to be more active than the conventional $\text{Cu}/\text{ZnO}/\text{Al}_2\text{O}_3$ catalyst for the CO_2 reduction to methanol at ambient pressure.^{71,72} A specific stoichiometric ratio (Ni_5Ga_3) was required in the catalyst formulation, which was stabilized by SiO_2 , to achieve high selectivity. Interestingly, redox-active In_2O_3 was also found to be a promising catalyst component with high methanol selectivity and remarkable stability due to its ability to form oxygen vacancies and metallic In in the reaction process.⁷³ Once the In_2O_3 catalyst was supported on ZrO_2 , its catalytic activity was further improved and the methanol

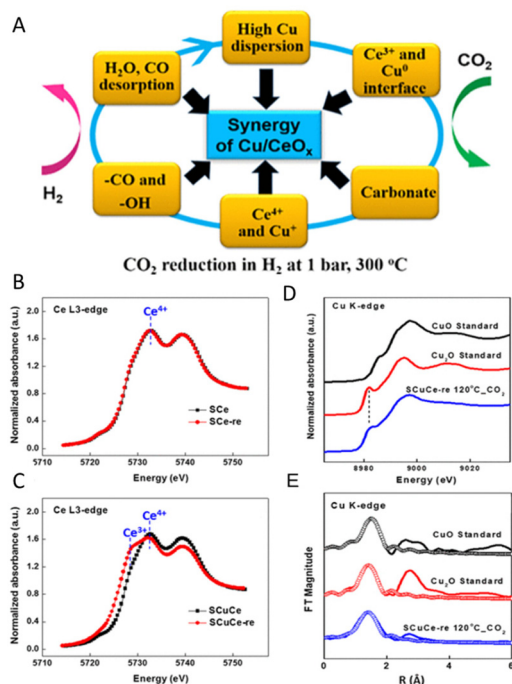


Fig. 11 (A) Schematic illustration of synergy of Cu/CeO_x for CO_2 hydrogenation. (B–E) XAS spectra of Cu and Ce oxidation state change during reaction (note that S_{Ce} = SBA-supported CeO_2 and S_{CuCe} = SBA-supported Cu– CeO_2). Adapted from ref. 61 with permission. Copyright 2018 American Chemical Society.

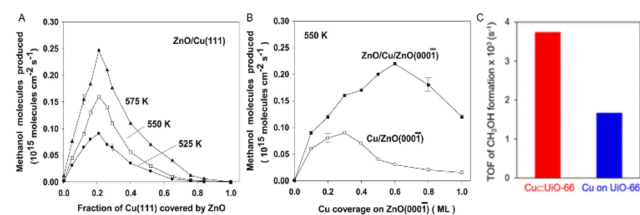


Fig. 12 (A, B) CO_2 conversion to methanol. (C) Initial TOFs of methanol formation over CuCuUiO-66 and Cu on UiO-66 . The reaction rates were measured after 1 h. Reaction conditions: 7 sccm of CO_2 , 21 sccm of H_2 , 10 bar, and 175 °C. Adapted from ref. 66 and 70 with permission. Copyright 2017 American Association for the Advancement of Science and 2016 American Chemical Society.

selectivity reached 99.8% with a CO₂ conversion of 5.2% and long-term stability of 1000 h under the industrially relevant reaction conditions.

3.2.3. Fischer–Tropsch reaction. The C₂₊ hydrocarbons, such as alkanes, olefins and liquid fuels, are important for today's chemical and energy industries. For example, olefins are currently produced on the order of 200 million tons per year and widely used in synthetic rubbers, plastics and cosmetics.⁷⁴ However, these hydrocarbons are traditionally generated from non-renewable fossil fuels, which results in large amounts of CO₂ emission.⁷⁵ Ideally, CO₂ can be used as a precursor for the synthesis of these hydrocarbons.⁷⁶

The FT reaction is a common route for the transformation of syngas (CO + H₂) to C₂₊ hydrocarbons. To achieve the direct hydrogenation of CO₂, two successive reaction steps need to be incorporated into one reaction system: the reduction of CO₂ to CO *via* RWGS reaction and hydrogenation of CO to hydrocarbons *via* FT reaction.⁷⁷ In the two-step reaction process, the CO conversion (up to 87%) is much higher than the CO₂ conversion (up to 45%). Therefore, improving the catalytic efficiency of the CO₂ conversion has been an important target.^{77–80} Fe-based catalysts have been widely used in CO₂ hydrogenation because of their high activity for both RWGS and FT synthesis.⁸¹ Fe catalysts with alkali metal promoters are reported to significantly enhance the selectivity towards long-chain hydrocarbons.⁸² These alkali metals, especially K, promote Fe catalysis by weakening the affinity with H₂ and enhancing the adsorption of CO₂ and CO intermediate.⁸³ Different promotional effects were observed by combining a Fe-based MOF catalyst with various elements (Fig. 13A).⁸³ K was found to enhance the olefin selectivity drastically from 0.7% to 36% (Fig. 13B).⁸³ CO₂ and H₂ chemisorption measurement showed that CO₂ uptake was enhanced while H₂ adsorption was weakened upon K addition, leading to stronger Fe–C interaction and higher selectivity toward olefins. The obtained C₂–C₄ olefin space time yields (STY) of the Fe/C + K (0.75) catalyst was among the best catalysts published (Fig. 13C).⁸³

In addition to alkali metals, transition metal components, such as Cu and Co components, were also found to promote Fe-catalysed CO₂ hydrogenation to hydrocarbons.^{84,85} Cu is known to be a highly active catalyst for methanol synthesis from CO₂, but when it combines with Fe, it enhances Fe catalysis for both RWGS and CO hydrogenation by suppressing CH₄ formation and promoting C₂–C₇ production.⁸⁴ The catalyst support is also an important factor to increase the selectivity for light olefins. For example, the ZrO₂-supported K–Fe (K–Fe/ZrO₂) catalyst exhibited much higher selectivity to lower olefins than the SiO₂-supported one;⁸⁶ the carbon-coated Fe-catalyst was much better dispersed and stabilized, and was highly active for the CO₂ conversion at atmospheric pressure with higher selectivity to C₂–C₄ olefins.⁸⁷ In addition, methanol has also been studied as a starting precursor for synthesis of olefins. It too requires two reaction steps: CO₂ hydrogenation to methanol and methanol conversion to hydrocarbons as described in recent reviews.^{88,89}

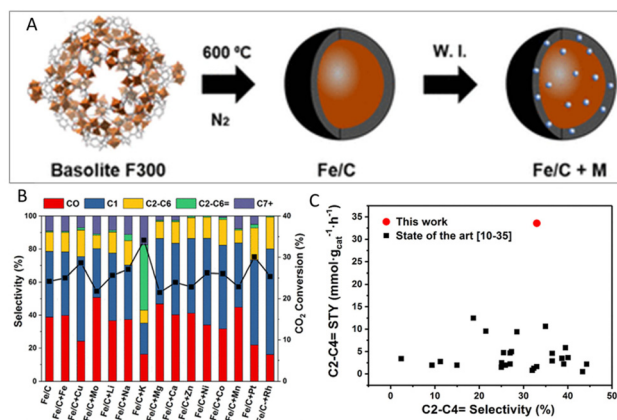


Fig. 13 (A) Synthetic strategy for the Fe-based catalysts by carbonization at 600 °C in N₂ and wetness impregnation (W. I.). (B) Effect of different promoters on CO₂ hydrogenation performance. (C) C₂–C₄ olefin space time yields (STY, mmol g_{cat}⁻¹ h⁻¹) obtained for the Fe/C + K (0.75) catalyst at 350 °C compared with the best catalysts available for CO₂ hydrogenation. Adapted from ref. 83 with permission. Copyright 2018 American Chemical Society.

Despite the great promise demonstrated from thermal reduction of CO₂ to value-added chemicals, these thermal reactions do require the use of high temperature and high pressure, which makes it challenging to stabilize the catalysts in the reaction conditions and to lower energy consumption.

3.3. Electrochemical reduction of CO₂

Electrochemical CO₂ reduction reaction (CO₂RR) is an appealing alternative to thermal reduction for converting CO₂ to value-added chemicals as the reaction can be promoted by renewable electricity under ambient conditions, and be catalysed more selectively by catalyst engineering, as illustrated in Fig. 14A.⁹⁰ The electrochemical CO₂RR on the surface of a metal catalyst is generally divided into three steps: CO₂ adsorption, charge transfer, and product dissociation. Each of these three steps plays an important role in controlling catalyst selectivity and final product distribution.⁹¹ The CO₂RR pathways have been studied extensively to understand various products detected from CO₂RR. Fig. 14B is just an example to show these complicated pathways leading to the formation of C₁ and C₂ products.⁹¹ The commonly accepted key reaction steps are CO₂ binding, protonation and reduction to *COOH, which can be further hydrogenated to form formate, or dehydrated to form CO that can either be released from the catalyst surface or function as a key intermediate for the next steps of hydrogenation and C–C coupling to C₁ and C₂₊ products. The mechanism leading to the formation of C₁ product is relatively simple. In contrast, the processes leading to C₂₊ products are much more complicated. Recent studies have focused on capturing and identifying the reaction intermediates, such as *COCO, *CHCHO, *COCO, that produce C₂₊ products.⁹²

3.3.1. Metal nanoparticle catalysis. Metal nanoparticles with large surface areas and controlled surface structures have been studied extensively as catalysts for CO₂RR.^{93–99} Fig. 15

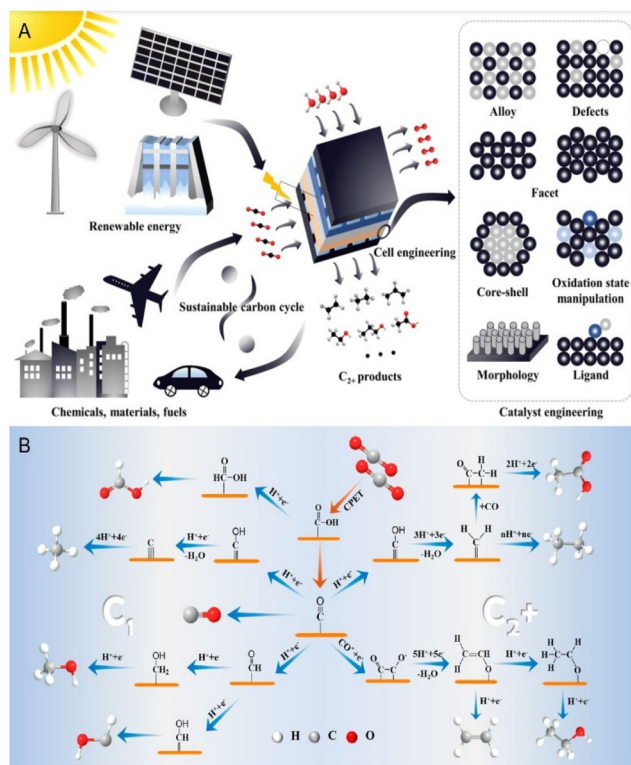


Fig. 14 (A) Schematic illustration of sustainable energy cycling based on electrochemical CO₂RR. (B) Proposed pathways for C₁ and C₂ + products from electrochemical CO₂RR. Adapted from ref. 90 and 91 with permission. Copyright 2020 American Association for the Advancement of Science, 2021 American Chemical Society.

(A)	Catalyst	FE	Potential
Au	Oxidize-derived Au film	96%	-0.35 V
	8-nm Au NPs	90%	-0.67 V
	2-nm wide Au NWs	94%	-0.35 V
	Au NPs-C ₂ N ₄	90%	-0.45 V
(B)	Catalyst	FE	Potential
	5-nm Ag NPs	84%	-0.75 V
	Ag nanotriangles	96%	-0.86 V
	Ag NWs/NC700	95%	-0.8 V
(C)	Ag NPs-C ₂ N ₄	90%	-0.85 V
	Catalyst	FE	Potential
(D)	3-nm Pd NPs	90%	-0.75 V
	Catalyst	FE	Potential
(E)	Cu/SnO ₂ core/shell NPs (0.8-nm shell)	93%	-0.7 V
	Catalyst	FE	Potential
(F)	Ni ₃ N NPs	85%	-0.90 V

Fig. 15 Summary of some representative nanocatalysts based on Au (A), Ag (B), Pd (C), Sn (D) and Ni (E) for electrochemical CO₂RR to CO. All potentials are vs. RHE. NP denotes nanoparticle and FE is the reported faradaic efficiency. Adapted from ref. 93 with permission. Copyright 2019 Cell Press.

summarizes some representative nanoparticle catalysts that are selective for CO₂RR to CO.⁹³ Ultrathin Au nanowires of about 2 nm in width and hundreds of nm in length were

found to be among the most active and selective catalyst for the CO₂ reduction to CO.⁹⁹ The CO selectivity is sensitively dependent on the length of the nanowires. The 500 nm Au nanowires showed the onset potential of CO₂ reduction to CO at -0.2 V (with 37% FE) but reached 94% FE and mass activity (1.84 A g_{Au}⁻¹) at -0.35 V. DFT calculation revealed that both COOH and CO preferentially bind to the edge site on the Au nanowires, with COOH binding marginally (0.04 eV) stronger than that on the Au(211) edge but CO binding 0.23 eV weaker than that on the Au₁₃ corner, suggesting that nanowire surface with maximal edge sites facilitates CO₂ reduction to COOH and further to CO.⁹⁹ In addition to Au, Ag, Pd, SnO₂-coated Cu, and Ni-N were also found to be selective in catalysing CO₂RR to CO, as summarized in Fig. 15.^{100–103} When Pd, In, Sn, and Bi nanoparticles were employed as catalysts for the CO₂RR, formate (HCOO⁻) was the main product.^{104–107}

Compared with the formation of CO and formate, selective reduction of CO₂ to C₂ products has been challenging, and Cu has been the major component that is required to catalyze the C-C formation.^{92,95} Recent studies have suggested that the key active components are Cu-Cu₂O mixtures, as observed in the CO₂RR studies on partially oxidized Cu electrode.^{108–111} Cu(I) and residual subsurface oxygen species are considered to play important roles towards enhanced performance. The oxidation state of Cu can be reversibly transformed between Cu(0) and Cu(I) under the electrochemical reaction conditions. The presence of Cu(I) and Cu(0) significantly improves the kinetic and thermodynamic processes of CO₂ activation and *CO dimerization. *In situ* spectroscopy studies, such as electrochemical liquid transmission electron microscopy (TEM), X-ray photoelectron spectroscopy (XPS) and XAS studies, have shown that the catalyst surface undergoes dynamic structural changes under CO₂RR conditions. For example, over the electroreduction time period, CuO nanosheets were seen fragmenting into smaller species and floating in the liquid layer (Fig. 16A).¹¹² *In situ* grazing incidence X-ray absorption spectroscopy (GIXAS) and X-ray diffraction (GIXRD) were also used to study thin Cu electrode (50 nm thick) and to characterize the near-surface structure of the electrode under the CO₂RR conditions (Fig. 16B and C).^{88,113} It was found that during the catalytic reaction, the surface of the polycrystalline Cu electrode was partially oxidized to Cu₂O. The co-existence of Cu(0) and Cu(I) on the catalyst surface during the CO₂RR was further proved by *operando* time resolved XAS.¹¹⁴ It is now commonly believed that there is a synergistic effect between Cu(0) and Cu(I), which promotes the C-C coupling of intermediates in the reaction process, favouring the formation of C₂₊ products. The role played by the Cu(I) effect in enhancing CO₂RR to hydrocarbons was further supported by the Cu₃N nanocube-catalysed CO₂RR for the formation of C₂H₄ as a major product.¹¹⁵ This high selectivity to C₂H₄ was attributed to the Cu(I) stabilization by N and Lewis basicity of N on the Cu(100) facet, facilitating C-C coupling and C=O/C-O hydrogenation.

3.3.2. Single-atom catalysis. Single-atom catalysts, with isolated metal atoms dispersed on conductive carriers, have

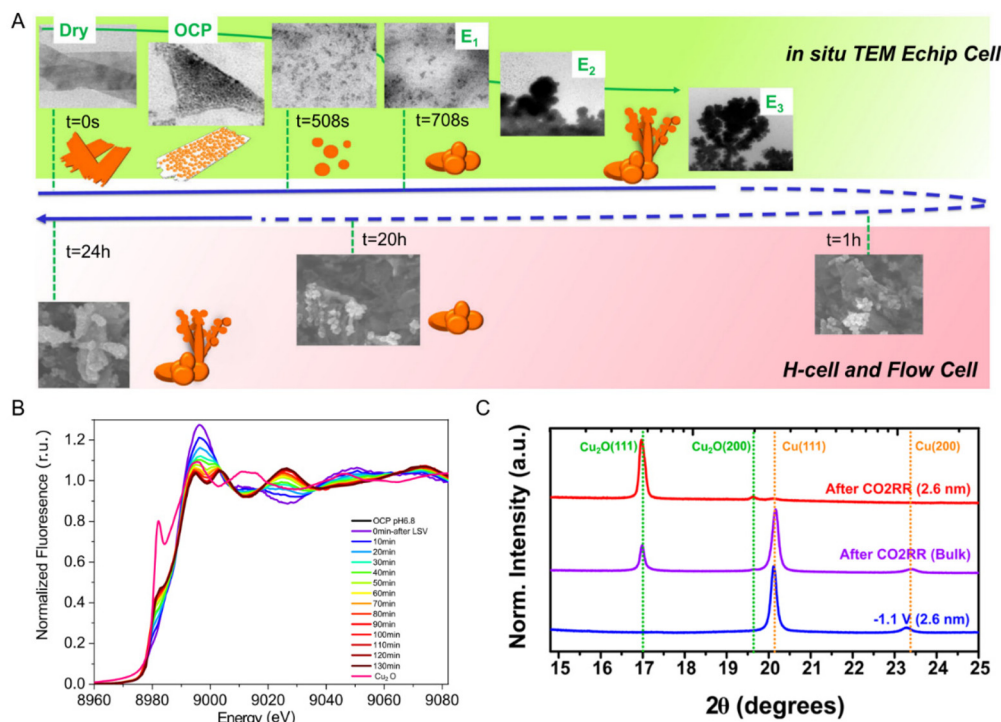


Fig. 16 (A) Schematic overview (timeline) of the experimentally observed evolution of the CuO nanosheet morphology probed by the *in situ* TEM E-chip flow cell, H-cell, and flow cell electrolyser. (B) XANES at the Cu K-edge of the CuO nanosheet catalyst after CO₂ reduction for different minutes. (C) Grazing incidence X-ray diffraction of Cu(pc) at a probe depth of 2.6 nm before and after releasing the applied potential. Adapted from ref. 112 and 113 with permission. Copyright 2020 American Chemical Society and 2021 Nature Publishing Group.

demonstrated excellent catalytic performance in many chemical reactions. These catalysts integrate the benefits of both homogeneous and heterogeneous catalysts, and provide an ideal platform for optimizing chemical reactions *via* their easily controllable coordination sites and electronic structures, strong metal–support interactions, as well as their maximal atom utilization. The electrochemical reduction of CO₂ over single metal atom sites can be traced back to the 1970s when cobalt and nickel phthalocyanines were first found to be active for CO₂ reduction.¹¹⁶ Since then, metal–organic complexes with well-defined M–N_x sites have been extensively studied for CO₂RR with high catalytic performance and durability.¹¹⁷ In these M–N_x structures, both C and N coordinated to M also show important synergy effects (*via* electronic polarization) on the M catalysis to facilitate CO₂ activation and further reactions. For example, C–Zn_xNi_y ZIF-8 catalysts with undercoordinated Ni–N_x sites ($x < 3$) showed much enhanced CO₂-to-CO activity and selectivity compared with the Ni–phthalocyanine one with well-defined Ni–N₄ sites.¹¹⁸ DFT calculations revealed that the free energy for *COOH formation was lower on the Ni–N_x sites than on the Ni–N₄ sites. This low coordination effect on catalysis enhancement was also observed from the Co–N catalysts.¹¹⁹ When the Co–N coordination number was decreased from 4 to 2 (Fig. 17A and B), the Co–N₂ sites showed the best CO₂RR performance with both high activity and selectivity towards the formation of CO (Fig. 17C and D).¹¹⁹ More and more single-atom catalysts are emerging to show

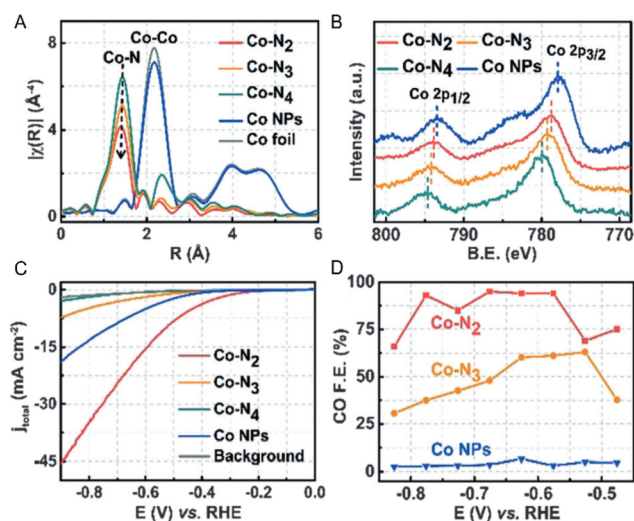


Fig. 17 (A) XAS spectra confirm the atomic dispersion of Co atoms in Co–N₂, Co–N₃, and Co–N₄, and suggest the lowest N coordination number in Co–N₂. (B) XPS of all four samples. (C) (a) Linear sweep voltammetry (LSV) of Co–N₂, Co–N₃, Co–N₄, and Co NPs and pure carbon paper as background. (D) CO faradaic efficiencies at different applied potentials. Adapted from ref. 119 with permission. Copyright 2018 Wiley-VCH.

promising catalysis for the CO₂ reduction to C-products beyond CO. These results have been nicely summarized in several recent reviews.^{117,120,121}

Up to now, various catalysts have been demonstrated to show promising catalysis for CO₂RR to value-added chemicals under ambient conditions. Their catalysis performance is better understood at the atomic scale, and many factors, including atomic composition, atom oxidation states and coordination environment, have been identified as important to improving catalysis activity and selectivity. Despite these advances, controlling catalytic CO₂RR to a C₂₊ product is still a challenging task due to the strong competition from the reaction pathways that lead to the formation of C₁ products. Key factors to maximize C₂₊/C₁ ratios need to be identified, and catalyst structures developed for such catalysis should also stay stable in the CO₂RR condition.

3.4. Catalyst–electrolyte interface engineering for CO₂ reduction

As electrochemical reactions occur at interfaces of catalysts and electrolytes, and as the CO₂RR needs the presence of protons to form hydrocarbons, interface engineering to control proton concentration and hydrophobicity is equally important for fast binding and reduction of CO₂. Recent advances in surface chemistry and spectroscopy also offer new opportunities to probe reaction mechanisms of CO₂RR at the interfaces and, in turn, guide the design of such interfaces for catalysis enhancement.^{122–125} Electrochemical systems that can be used to optimize gas transport,^{126–129} electrolyte functions,^{130–133} intermediate detection,^{134–139} and reaction pathway engineering,^{140–142} have been rapidly developed to improve the overall catalytic performance. In this section, we highlight how interfacial engineering can be applied to optimize electrolyte and catalyst surface ligand effects to enhance CO₂RR catalysis.

3.4.1. pH gradient, cation, and anion effects. Most electrocatalytic CO₂RRs are operated in an electrochemical reaction system with aqueous electrolyte. The electric double layer formed between the electrolyte and the electrode contains key intermediate species that can dominate the mass transport and catalytic evolution process of CO₂.¹⁴³ A number of parameters can be chosen to optimize the electric double layer structure and to control the local environment on the catalyst surfaces, including electrolyte buffer capacity,¹⁴⁴ anion/cation types and concentrations,¹⁴⁵ localized pH,¹⁴⁶ and proton/CO₂ accessibility.^{147,148} Therefore, the selection of an appropriate electrolyte is of critical importance to tune the CO₂RR activity and selectivity. For example, when operating in an aqueous electrolyte, the reduction of protons, commonly known as the hydrogen evolution reaction (HER), competes with CO₂RR; and it, in turn, lowers the overall electrocatalytic efficiency towards CO₂RR.¹⁴⁹ However, because of the continuous consumption of protons through proton-coupled CO₂RR and HER, the accumulation of OH[−] near the surface of a catalyst results in a higher local pH, creating a pH gradient between the interfacial area of the catalyst and electrolyte.¹⁵⁰ The presence of this pH gradient can affect mass transport of different reaction species, such as OH[−], CO₂, HCO₃[−] and CO₃^{2−}, and as a result, dominate the reactions pathways.^{144,146,151}

The CO₂RR selectivity can be improved by increasing the CO₂ concentrations and by inhibiting the HER near the electrode–electrolyte interfaces. Due to the relative low solubility of CO₂ in aqueous electrolyte, a high local pH is required to increase the local CO₂ concentration and to suppress HER.¹⁵² This was better demonstrated when a mesoporous Au-inverse opal (Au-IO) structure served as the catalyst for CO₂RR. In the CO₂RR condition, the partial current density related to CO₂RR was increased with reduction potentials regardless of the thickness of the Au-IO film (Fig. 18A), while that related to HER was decreased initially before increase only slightly at more negative potentials, and, more importantly, the thicker the Au-IO film, the smaller the partial current density (Fig. 18B).¹⁵³ Here a beneficial pH gradient was created in the pores of the Au-IO film, which enhanced CO₂ adsorption and conversion to CO, but limited proton diffusion and HER (Fig. 18C).¹⁵³ This was further confirmed by *in situ* electrochemical analysis, showing the pH changes near the electrode surfaces.^{150,154} Another way of promoting CO₂RR is to increase the CO₂ pressure, and therefore the CO₂ concentration, as demonstrated in the Cu-catalysed CO₂RR to ethylene (FE 44%) when the CO₂ pressure was set at 9 atm during the electrolysis.¹⁵⁵ This improved selectivity to ethylene was attributed to the increase in *CO concentration in the initial catalysis steps, promoting *CO–*CO coupling and hydrogenation.

Metal cations would accumulate near the surface of electrodes under reductive potentials, forming an electric double layer, which could affect the mass transport of CO₂. As shown in Fig. 19A, the constructed electrode–electrolyte interface is assigned to the inner Helmholtz plane (IHP) within which intermediate species are populated, and outer Helmholtz

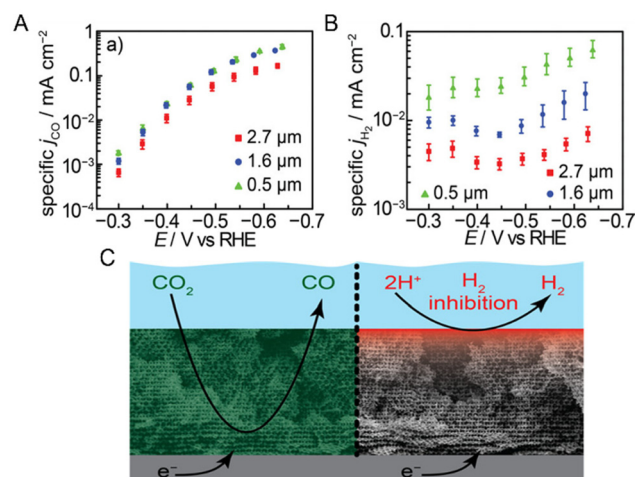


Fig. 18 Specific activity for CO (A) and H₂ (B) with different thickness of Au-IO: 0.5 μm (green triangles), 1.6 μm (blue circles), and 2.7 μm (red squares). The samples were evaluated in CO₂-saturated 0.1 M KHCO₃ electrolyte, pH 6.7. Error bars represent standard deviations of three independently synthesized Au-IO samples for each thickness. (C) Scheme represents the mesostructure-induced pH gradient during CO₂RR. Adapted from ref. 153 with permission. Copyright 2015 American Chemical Society.

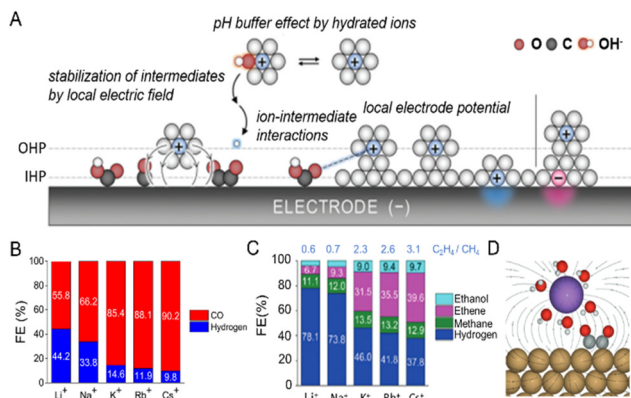


Fig. 19 (A) Simplified schematic illustration of the electric double layer composed of the inner Helmholtz plane (IHP) and outer Helmholtz plane (OHP) with chemical equilibria involved. (B) Faradaic efficiencies (FEs) for CO and H₂ produced over Ag at -1 V vs. RHE in CO₂-saturated 0.1 M MHCO₃ (M = Li, Na, K, Rb, Cs) electrolyte. (C) Faradaic efficiencies (FEs) for C₂H₅OH, C₂H₄, CH₄, and H₂ produced over Cu at -1 V vs. RHE in CO₂-saturated 0.1 M MHCO₃ (M = Li, Na, K, Rb, Cs) electrolyte. (D) Schematic illustration of the local electric field created by cation at the catalyst interface and stabilized OCCO intermediate. Adapted from ref. 143, 156 and 157 with permission. Copyright 2020 Royal Society of Chemistry and 2016, 2017 American Chemical Society.

plane (OHP) beyond which the hydrated cations are present.¹⁴³ Under a reductive potential, the hydrated cations are attracted to the electrode surface due to the Coulomb attraction, participating in the chemical reactions, modifying the catalyst surface electronic structure, and even blocking active sites on the catalyst surface. Therefore, the catalytic performance of a catalyst on CO₂RR can be highly dependent on the electrolyte. For example, when a Ag electrode was studied for CO₂RR to CO, it was found that CO FEs were only around 40% when the Li⁺- and Na⁺-based electrolyte was used as the reaction medium, but the FEs reached 85–90% when the electrolyte contained a larger cation, such as K⁺, Rb⁺ or Cs⁺ (Fig. 19B).¹⁵⁶ Compared with smaller cations, which are strongly hydrated, the larger cations are weakly hydrated and more accessible to the surface of the electrode, leading to the decrease in their pK_a and increase in the localized CO₂ concentration. A similar cation size effect was also observed when a Cu electrode was studied for CO₂RR in 0.1 M MHCO₃ electrolyte. Increasing the cation size from Li⁺ to Cs⁺ in the electrolyte, the FE for H₂ was decreased, but the FE for C₂H₄ and C₂H₅OH was increased (Fig. 19C).¹⁵⁷ It was believed that the larger cations helped to stabilize the polar species, such as *CO₂, *CO, and *OCCO, more efficiently in the reduction condition, favouring their further coupling and hydrogenation (Fig. 19D). As a comparison, CH₄ FE was rarely affected by the cation sizes due to the negligible cation interaction with the nonpolar *H and *CHO intermediate species.

Similarly, anions in electrolytes can also affect the CO₂RR performance of metal catalysts. These anions, for example halides, can function as soft bases to bind to Au and Cu strongly to modify the catalyst surface structure or morphology

during the CO₂RR, as demonstrated in the CO₂RR catalysis of plasma-activated Cu foil.¹⁵⁸ It was found that I⁻ ions enhanced the reactivity dramatically (lowered the onset potential) as compared with Br⁻ and Cl⁻ ions, and the total FE for C₂–C₃ products (ethylene, ethanol, and propanol) reached 65% at -1.0 V (vs. RHE). I⁻ ions were thought to be strongly adsorbed on the electrode surface, enhancing the CO₂ binding through the formation of I⁻–C bonds. Anions can also regulate the pH change near the catalyst surface, affecting the catalyst's CO₂RR performance.¹⁵⁹

3.4.2. Surface ligand effects. Adding ligands on the surface of catalysts offers a powerful way to control the interface of catalyst–electrolyte.¹⁶⁰ The inspiration is from nature where the catalytic efficiency of metalloenzymes heavily relies on the coordination environment of metal sites, e.g., protein frameworks in both first and second coordination spheres. Protein frameworks, despite not being catalytically active by themselves, are an essential component in tuning the activity and selectivity of metal sites. Modifying metal catalysts with surface ligands, therefore, can also enhance electrocatalytic performance toward CO₂RR. Such modification is usually achieved by covalent or non-covalent binding of organic surfactants to metal surfaces.^{161–164} Surface ligands can boost the intrinsic catalytic activity of metal catalysts by reducing CO₂ activation barriers,^{165–167} by changing mass transport during CO₂RR,^{168–170} and/or by defining the local environment to suppress byproduct formation (e.g., HER).¹⁷¹

The common organic ligand used for metal surface modification is thiol in the form of R–SH, where R represents an organic substituent. –SH has strong bonding affinity with all catalytically active metal surfaces. –S⁻ is a softer base than –O⁻ and can bind to a Group 10 or 11 metal even more strongly to impact its catalysis for CO₂RR.¹⁷² There have been numerous studies in modifying catalyst surfaces with thiols to improve the CO₂RR selectivity.^{168,173,174} One example is to modify a polycrystalline Au film electrode with three different thiols, 2-mercapto-propionic acid (MPA), 4-pyridylethylmercaptan (4-PEM), and cysteine (CYS), and to study the thiol effects on the Au catalysis for CO₂RR.¹⁷⁵ Such modifications did not improve Au catalysis for CO₂RR to CO (the surface coverage generally reduced the Au catalysis selectivity to CO), but they changed other parts of the Au catalysis: the 4-PEM-modified Au showed improved selectivity to formate (from 10% FE on Au to 22% on PEM-Au), while the MPA-modified Au showed nearly 100% FE towards H₂ and the CYS-modified Au was more active (not more selective) for generating CO and H₂. These Au catalysis changes upon the surface modifications were attributed to the proton-induced desorption mechanism associated with pK_a of the thiol ligands, as illustrated in the 4-PEM-modified Au catalysis for the improved selectivity to formate (Fig. 20A), in which 1e⁻ reduction of pyridine to pyridinium also helped to bind and reduce CO₂ to facilitate the second proton binding to CO₂ and its conversion to formate.¹⁷⁶ Not surprisingly, MPA with the smallest pK_a promotes HER.

Another example is to use the thiol-terminated imidazolium to improve Au catalysis for the formation of ethylene glycol

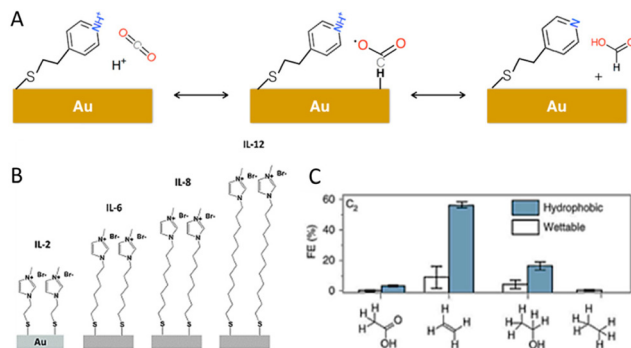


Fig. 20 Comparison of partial current density and FE for thiolate ligands on polycrystalline Au: (A) proposed reaction mechanism of the formate production at 4-PEM and Au interfaces. (B) Schematic of Au electrodes with 1-methylimidazolium-terminated SAMs (IL-2, IL-6, IL-8, and IL-12). (C) FE of C₂ products on both wettable and hydrophobic Cu dendrites at the total current density of 30 mA cm⁻². Adapted from ref. 175, 171 and 168 with permission. Copyright 2017 American Chemical Society, 2015 Royal Society of Chemistry and 2019 Nature Publishing Group.

(CH₂OH)₂.¹⁷¹ When the Au electrode was modified with different imidazolium-SH ligands (Fig. 20B), the Au catalysis showed the ligand length-dependent CO₂RR catalysis selectivity with 1-(2-mercaptoethyl)-3-methylimidazolium bromide (IL-2)-modified Au exhibiting highest FE (87%) towards ethylene glycol.¹⁷¹ Such enhancement in selectivity to ethylene glycol was attributed to more efficient coupling of imidazolium aldehyde intermediates in the reaction condition. In the presence of a longer ligand chain on the Au surface, the interaction between imidazolium and Au gets weaker, limiting the charge transfer for the formation imidazolium aldehyde intermediates.

Surface ligand modification can also be used to control the microenvironment of catalytic sites and to impact catalysis efficiency. When modifying the catalyst surface with a hydrophobic ligand, the surface area becomes hydrophobic, which allows CO₂ to accumulate, creating a triphasic interface of gas-electrode-electrolyte.¹⁶⁸ For example, when modified with 1-octadecanethiol (ODT), the Cu dendritic surface became superhydrophobic with a water contact angle of 153°. Such a hydrophobic dendrite entrapped more CO₂ near the Cu surface, more efficiently improving the Cu catalysis of CO₂RR to C₂ products (Fig. 20C).¹⁶⁸

Amine ligands have also been broadly used not only to stabilize metal NPs in their synthesis but also to modify metal surfaces for catalysis improvement.^{98,99,177-181} The presence of amine groups at metal surfaces provides numerous Lewis base centers that can further improve CO₂ adsorption near these metal surfaces *via* the amine-CO₂ interaction.¹⁸² The amine ligand effect was well demonstrated in a comparative study of Ag catalysis for CO₂RR once a Ag electrode was modified separately with oleylamine (OLA), oleic acid (OA) and 1-dodecanethiol (DDT). The OLA-modified Ag was found to show the highest selectivity to CO (FE 94.2%) across a broad range of potentials, while the OA- and DDT-modified Ag demonstrated

only 89.1% and 71.0% FE_{CO}, respectively (Fig. 21A).¹⁸³ In studying the amine ligand effect on Au catalysis for CO₂RR, Au NPs supported on graphene oxide (rGO) were grafted with propylamine (PA), hexylamine (HA), OLA, ethylenediamine (EDA) or polyethyleneimine (PEI), respectively.¹⁸² It was found that amines with a linear structure favored the CO₂RR to CO, and the longer the chain, the higher the CO FE (Fig. 21B).¹⁸² As a comparison, bulky branched amines can block the catalyst's active sites and prevent CO₂ from interacting with the metal surface, lowering the CO₂RR selectivity.

Despite the evident effect of these thiols/amines on metal catalysis, the long-standing catalyst stability issue in the CO₂RR condition remains. To stabilize the NP catalysts more efficiently in the CO₂RR condition, N-heterocyclic carbene (NHC) ligand has been introduced.^{162,164,184,185} NHCs bind with metals through the lone electron pair on C to form a strong C-metal σ bond,¹⁸⁶⁻¹⁸⁸ which has been applied to modify the surfaces of a variety of metals.^{189,190} More importantly, the σ-donation of NHCs enriches the charge density on metal surfaces, further promoting metal binding with electrophile CO₂.¹⁸⁶ For example, Au NPs modified with sterically bulky 1,3-bis(2,4,6-trimethylphenyl)imidazol-2-ylidene (Cb) (Fig. 22A) showed a much higher FE_{CO} (83%) and current density (7.6-fold) than the plain Au NPs (FE_{CO} = 53%) at the potential of -0.57 V.¹⁶⁴ The tridentate NHC ligand timtmb^{Me} (Fig. 22B)-modified Pd electrode showed not only high selectivity for CO₂RR but also stability.¹⁹¹ In the presence of timtmb^{Me}, the Pd catalyst exhibited a larger total current density and positively shifted onset potentials relative to the parent palladium foil (Fig. 22C).¹⁹¹ The onset potential for CO₂RR appeared at -0.12 V, which is about 265 mV, positively shifted relative to that of the unmodified Pd. The FE of C₁ products increased from the initial 23% to 86% (with timtmb^{Me}, 82% of formate and 4% of CO, Fig. 22D) at -0.57 V vs. RHE with a 32-fold increase in current density.¹⁹¹ The tridentate NHC-modified Pd also showed much improved stability as evidenced from the steady product FE in the 6 h electrolysis period.

Metal catalysts modified with polymer NHCs have shown significant catalytic enhancement in CO₂RR. While small-molecule ligands can vary the surface properties, polymer

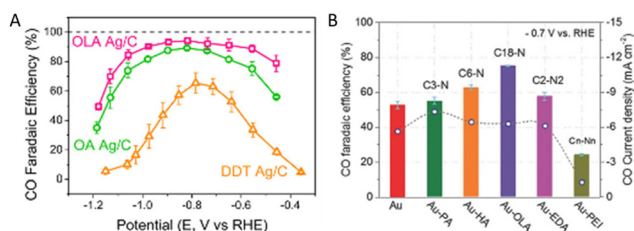


Fig. 21 (A) FE_{CO} of OLA-, OA- and DDT-modified Ag NPs supported on carbon black (Ag/C). (B) FE_{CO} (column) and CO current density (circle) of different Au catalysts at -0.7 V (vs. RHE). Adapted from ref. 183 and 182 with permission. Copyright 2017 American Chemical Society and 2018 Wiley-VCH.

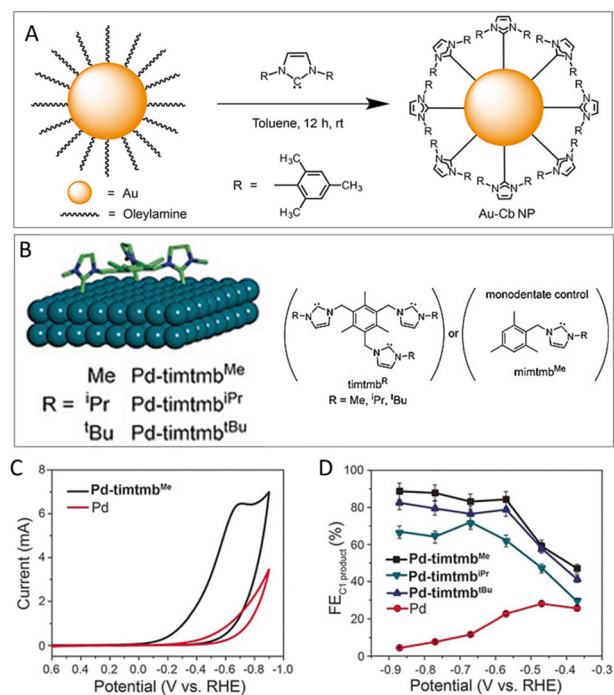


Fig. 22 (A) Surface modification of Au NPs with 1,3-bis(2,4,6-trimethylphenyl)imidazol-2-ylidene (Cb) through ligand exchange. (B) Schematic illustration for the tripodal NHC functionalization of Pd surfaces. (C) CV scans of Pd and Pd-timtmb^{Me} electrodes in CO₂-saturated 0.5 M KHCO₃ at pH 7.3. (D) FE of C1 products (CO for unmodified Pd; HCOO⁻ and CO for tripodal NHC-modified Pd) on unmodified Pd electrodes and tripodal NHC-modified Pd electrodes at different potentials. Adapted from ref. 164 and 191 with permission. Copyright 2016 American Chemical Society and 2018 John Wiley and Sons Ltd.

ligands form a protective coating layer of 10–50 nm that could “gate” the accessibility of catalytic metal NPs. Monodentate and multidentate polymer NHC ligands were first studied to stabilize metal catalysts under reductive potentials and to improve the CO₂RR selectivity.¹⁶² The multidentate polymer NHC ligand poly(vinylbenzyl *N*-methylbenzyl *N*-heterocyclic carbene) (PVBMB-NHC₅₇, P1) was synthesized using quaternization of *N*-methyl benzimidazole with poly(vinylbenzyl chloride) (PVBC). The monodentate NHC-terminated polystyrene (PS₆₅-NHC, P2) was prepared from the end-group functionalization of the halogen-terminated one through atom transfer radical polymerization (ATRP). After counterion exchange with KHCO₃, the two imidazolium-ended polymers could graft to Au NPs (~14 nm) at relative high grafting density, 1.3 and 0.9 chains per nm² for P1 and P2, respectively (Fig. 23A).¹⁶² When catalysing the CO₂RR, the Au-P1/C and Au-P2/C showed both higher activity and selectivity than the Au/C due to their more efficient role in suppressing HER (Fig. 23B).¹⁶² The polymer-modified Au NPs also demonstrated much improved stability, as shown in the change of the electrochemical active surface area (ECSA) of Au NPs during a 2 h electrolysis at -0.9 V (Fig. 23C).¹⁶² The citrate-capped Au NPs showed only 24.7% ECSA retention after the 2 h electrocatalysis, while the polymer

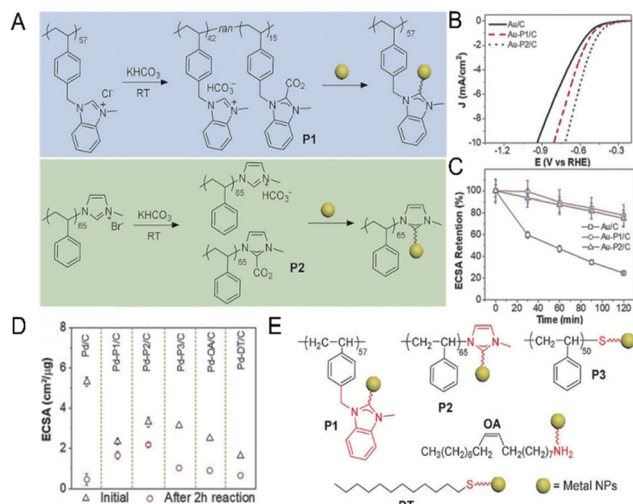


Fig. 23 (A) Schematic illustration of synthesis of P1, P2 and surface modification of NPs (yellow). (B) LSV curves measured in 0.1 M KHCO₃ at a scan rate of 10 mV s⁻¹ for all three samples. (C) ECSA retention at -0.9 V for different electrolysis times of NHC-modified Au NPs. (D) ECSA of Pd catalysts before and after CO₂ reduction at -1.26 V for 2 h with various ligands as shown in (E). Adapted from ref. 162 with permission. Copyright 2019 John Wiley and Sons Ltd.

NHC-modified Au NPs had ~75% ECSA retention. Even after 11 h electrolysis, the Au-P1/C still had a FE_{CO} of 86% while the unmodified Au NPs only had <10% FE_{CO} left. The polymeric NHC-binding strategy could be applied to Pd/C (Fig. 23D), which showed the desired enhancement in both selectivity (FE_{CO} was increased from 45% to 60%) and stability (ECSA retention was improved from 10% to 91% after 2 h electrolysis).¹⁶² As a control, Pd/C modified with thiol-terminated PS ligands and other ligands (Fig. 23D and E)¹⁶² were all less stable than the Pd/C modified with polymer NHC.

Very recently, a nanoparticle/ordered-ligand interlayer (NOLI) was proposed and applied to enhance CO₂RR efficiency.¹⁶⁹ The NOLI structure was created by the collective dissociation of bound ligands (alkylphosphonate) from a dense assembly of metal (Au, Ag or Cu) NPs. Under the reductive potentials, covalently bonded ligands detached but were maintained on the surface through the non-covalent interactions between ligands in the densely packed assembly, as illustrated in Fig. 24A.¹⁶⁹ Consequently, this allows K⁺ to transport onto the catalyst surface to balance the overall charge, creating a pseudocapacitive pocket interlayer. Specifically, the ligand chains form a hydrophobic domain around the pocket that facilitates the diffusion of CO₂, while inhibiting the diffusion of water/protons, into the NOLI structure, favouring CO₂ conversion over the HER.¹⁹² The Ag-NOLI improved the activity and selectivity towards CO formation dramatically in CO₂RR, whereas the turnover and selectivity drop to a level similar to Ag foil when the ligand layer was removed (Fig. 24B and C), supporting the importance of the NOLI structure in

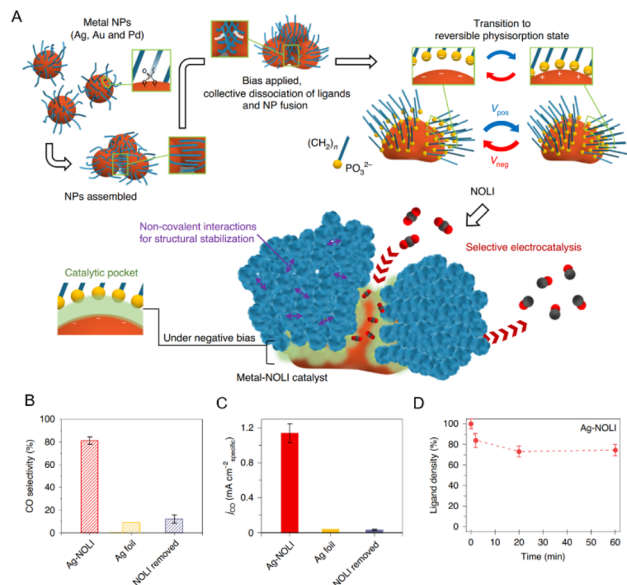


Fig. 24 (A) Formation of a NOLI and a metal–NOLI catalyst for selective electrocatalysis. Blue chains on the metal NPs represent chemically bonded alkylphosphonic ligands. Upon applying a negative bias on the assembled NPs, the ligands collectively dissociate from the metal surface during NP fusion and transit to a reversible physisorption state (explicitly shown by the emphasized yellow phosphonate head group). V_{pos} and V_{neg} indicate a positive (anodic) and a negative (cathodic) polarization of the metal particles, respectively. The ligand layer maintains its stability through the non-covalent interactions of the alkyl tails (blue) in an ordered configuration (indicated by the purple double-headed arrows). The resultant metal–NOLI catalyst provides a unique catalytic pocket for selective CO_2 electro-conversion (C, black; O, red). (B) CO selectivity and (C) specific current density of Ag–NOLI, Ag foil and Ag particles after the NOLI is removed from Ag–NOLI, at -0.68 V vs. RHE. (D) Ligand density of Ag–NOLI estimated from XPS throughout CO_2 electrolysis. Adapted from ref. 169 with permission. Copyright 2021 Nature Publishing Group.

the selective CO_2 -to- CO transformation.¹⁶⁹ This NOLI structure was demonstrated to be highly active and selective across several metals with up to 99% CO selectivity and onset overpotentials as low as 27 mV. Interestingly, even without strong chemical binding, the ligand density (with respect to the NP surface area) remains relatively stable throughout electrolysis (Fig. 24D).¹⁶⁹ DFT calculations reveal that the specific configuration for the NOLI facilitates the bending of the adsorbed CO_2 molecule, thus promotes the rate-limiting step of the polarization of non-polar CO_2 with an electron transfer to form the intermediate $^*\text{CO}_2^{\cdot-}$.

4. Coupled CO_2 capture and conversion

Both CO_2 capture and CO_2 conversion processes are considered as promising strategies to reduce CO_2 emissions, therefore mitigating global warming and other associated environ-

mental concerns. However, most of the present CO_2 reduction studies, either thermal or electrochemical conversion, are based on pure CO_2 as the feedstock, and there exist large gaps between the capture and conversion processes. In a conventional CO_2 capture and conversion process, CO_2 is first captured from either ambient air or flue gas by various capture technologies. Then CO_2 is desorbed, compressed and utilized in the preparation of value-added products by chemical reduction reactions.¹⁹³ From the perspective of the whole system, however, the desorption and compression steps are energy-intensive, imposing a large energy penalty on the processes of CO_2 capture and conversion.¹⁹⁴ Therefore the combination of CO_2 capture and conversion has been suggested in a single integrated CO_2 capture and utilization process. The energetics comparison between independent and coupled CO_2 capture and conversion processes is shown in Fig. 25.¹⁹⁵ Dilute CO_2 can be captured through the formation of CO_2 -X adduct for both processes; however, the independent one requires an additional regeneration step to produce pure CO_2 for electrocatalysis, causing an extra capture “overpotential” energy. If both pathways have the same energetic level for CO_2 RR intermediates, integrated configurations could achieve lower overall energy requirements due to the energy saving through bypassing the capture media regeneration step. Therefore, integrating the capture and conversion processes is critical to decrease the cost and make the overall process energy efficient.

To date, coupling between CO_2 capture and conversion *via* thermo- and electro-catalysis has been studied only in a few reports. Therefore, this section summarizes the recent progress made in these two catalysis areas. The integrated capture and conversion were first demonstrated in 2013.¹⁹⁶ In the report, polyamines and amidine bases were used for CO_2 capture in

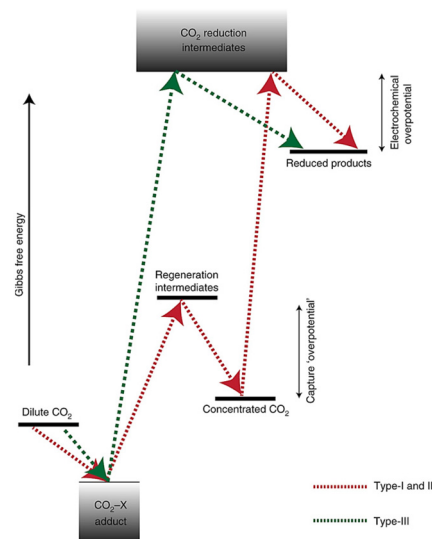


Fig. 25 CO_2 capture and conversion energetics for type-I and II (red) and type-III (green). Adapted from ref. 195 with permission. Copyright 2021 Nature Publishing Group.

alcohol solvents, and the capture products were subsequently hydrogenated to obtain alkylammonium formate salts by a Ru-based homogeneous catalyst at 40 bar H₂. The best conversion performance was achieved when CO₂ was captured by 1,5-diazabicyclo [4.3.0] non-5-ene and glycol to form alkyl carbonate, which was then reduced to formate with 55% yield. It should be noted that the captured CO₂ can facilitate hydrogenation and yield better performance in comparison with equivalent free gaseous CO₂, indicating the CO₂ activation upon capture with amines. CO₂ could also be captured by amines in aqueous media and subsequently converted to alkylammonium formate salts (Fig. 26A).¹⁹⁷ The major advancement of this capture/conversion system over the previously reported one is the use of a biphasic solvent, shown in Fig. 26B. CO₂ can be captured as carbamate or bicarbonate in aqueous amine solution, while the catalyst is dissolved in an organic solvent. This allows easy separation of the catalyst and formate product, and higher reaction rate due to good solubility of the captured CO₂ in water. The captured CO₂ was selectively converted to formate (up to 95% yield) in the presence of homogeneous Ru- and Fe-based pincer complexes.

Recently, the coupled capture and conversion further led to the synthesis of methanol at a 79% yield.¹⁹⁸ In this process, CO₂ was captured by a short-chain polyamine, pentaethylenhexamine (PEHA), to form ammonium carbamate and bicarbonate, which was further hydrogenated at 155 °C and 50 bar of H₂ for 55 h in the presence of a pincer Ru-complex catalyst (Fig. 27A). It should be noted that formate and formamide are essential intermediates for amine-assisted hydrogenation of CO₂ to CH₃OH. Similarly, alcohol-assisted CO₂ hydrogenation to methanol *via* formate ester has also been studied extensively, and was further extended to a new approach of CO₂ capture and conversion to methanol *via* alkali-metal hydroxides in ethylene glycol (Fig. 27B).¹⁹⁹ Different from amines, hydroxides do not suffer from volatility and oxidative degradation issues. More importantly, due to their high CO₂ affinity, these hydroxides have high efficiency for direct air capture of CO₂. In the one-pot system, CO₂ from atmospheric air was efficiently captured by an ethylene glycol solution of

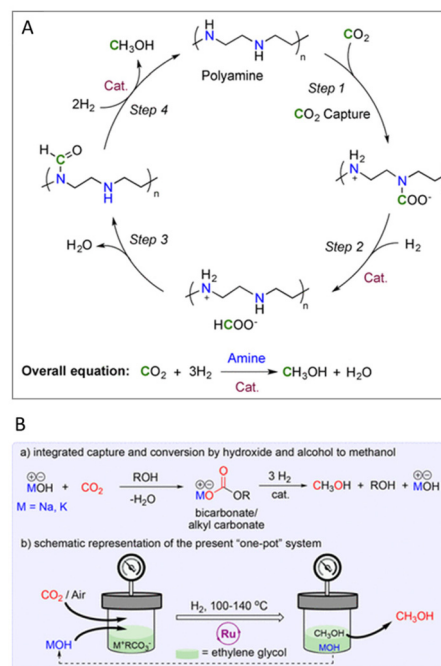


Fig. 27 (A) Cycle for CO₂ capture by an amine and conversion to methanol. (B) Integrated CO₂ capture and conversion system. Adapted from ref. 198 and 199 with permission. Copyright 2016 and 2020 American Chemical Society.

KOH to form alkyl carbonate intermediate, which was hydrogenated at 140 °C and 70 bar of H₂ for 72 h to form to methanol at a 100% yield. Such a high yield synthesis of methanol was attributed to the facile hydrogenation of the ester intermediate. Also in the process, hydroxide was partially re-generated and could be used for the next round of CO₂ capture and conversion.

In the case of combining capture and electrocatalysis, CO₂ can be captured by an aqueous solution of inorganic hydroxides to yield corresponding bicarbonates. Even though bicarbonate is commonly used as electrolyte for conventional CO₂ electrolysis, it can also serve as the carbon precursor for electrochemical reduction. So far, direct electrolysis of bicarbonate has not been reported yet, but the indirect electrochemical reduction reaction of bicarbonate solution has been achieved using a bipolar membrane (BPM) as the ion-exchange membrane in a flow cell where bicarbonate could be converted to molecular CO₂ due to local acidification.²⁰⁰ Electrolysis of the N₂-saturated 3.0 M KHCO₃ solution yielded CO with a FE of 81% at 25 mA cm⁻², which is comparable to the conventional gaseous CO₂ electrolysis in bicarbonate solution. Similarly, amines were used to capture CO₂ to form carbamate adducts.²⁰¹ Electrolysis of the CO₂-saturated 30% (w/w) monoethanolamine (MEA) aqueous solution led to the formation of formate with FE reaching up to 60.8% in the presence of a porous Pb electrode and cetyltrimethylammonium bromide. One challenge associated with the direct electrolysis of carbamate is the electrostatic repulsion between carbamate ion and the cathode surface. To address this issue, an alkali cation

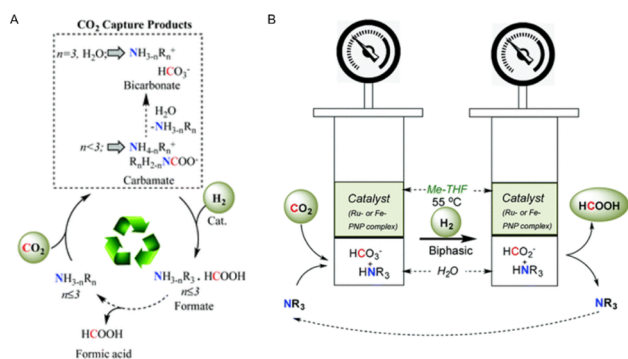


Fig. 26 (A) CO₂ capture and conversion to HCOOH. (B) Catalyst recycling by phase separation. Adapted from ref. 197 with permission. Copyright 2016 Royal Society of Chemistry.

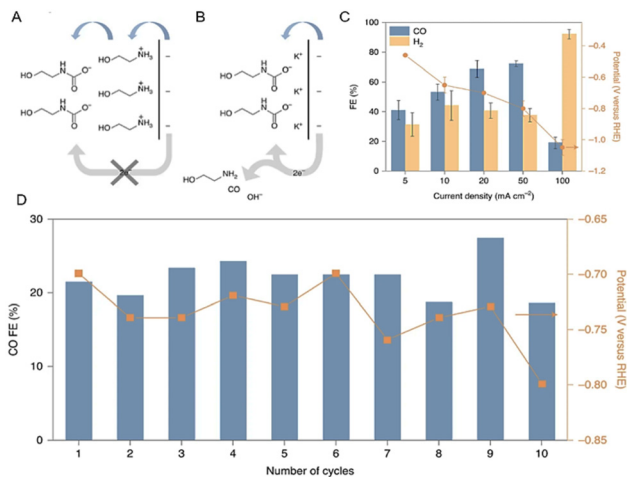


Fig. 28 (A) Proposed interfacial structure near the electrode surface. (B) Product distribution of MEA-CO₂ conversion to H₂ and CO at different applied current densities, ranging from 5 mA cm⁻² to 100 mA cm⁻² in a flow cell system. The error bars represent the standard deviation of three independent measurements. (C) Recycling performance of the 2 M MEA with 3 M KCl electrolyte at a constant applied current density of 10 mA cm⁻² heated to 30 °C in a three-electrode configuration. Products were collected within 1 h. Adapted from ref. 202 with permission. Copyright 2021 Nature Publishing Group.

could be added into the aqueous MEA solution to change the interfacial structure near the electrode, thereby improving the electron transfer from the electrode to the carbamate and the electrochemical performance, as shown in Fig. 28A and B.²⁰² For example, adding 2 M KCl as supporting electrolyte and by using Ag as a catalyst, CO was formed at 72% FE and a current density of 50 mA cm⁻² (Fig. 28C). The amine electrolyte was recycled 10 times and could still be used for the capture and conversion reaction without obvious FE_{CO} drop, demonstrating the promising stability of the electrolyte for continuous CO₂ capture and conversion (Fig. 28D).

5. Concluding remarks

A sustainable carbon cycle is essential for maintaining the healthy evolution of life globally. However, human activities, especially the ever-demanding energy consumption, have led to excessive depletion of fossil fuels, and severely affected the well-established equilibrium of the carbon cycle in nature. Given the threat of excessive CO₂ emission, there is now a growing demand for negative carbon technologies. Carbon capture and storage as well as direct air capture are promising technologies that could be utilized to minimize and/or reduce CO₂ emissions. Various adsorbent materials have been developed for CO₂ capture, including aqueous hydroxides, solid alkali carbonates, organic amines, and porous materials. To date, the investigations of direct air capture adsorbents have focused more on the use of solid-supported amine materials for improved stability and recyclability. The chemical reactions between CO₂ and amines ensure significant CO₂ uptake even

at low CO₂ partial pressures with much higher selectivity. The physical adsorption strategy using porous materials is also considered as an attractive alternative to conventional chemical adsorption approaches. Moreover, the modification of metal centres and functional groups as well as pore sizes could incorporate both chemisorption and physisorption capability within one adsorbent structure, and in turn offer better CO₂ adsorption capability and selectivity. Looking into the future, practical CO₂ adsorbent materials that are highly active, selective, recyclable, and cost-effective are still in demand.

The reduction of CO₂ into value-added chemicals and fuels is equally important to carbon neutral and sustainable energy. Thermal catalysis of CO₂ hydrogenation has been attractive because H₂ can be generated from water electrolysis by renewable energy. However, this method does require high temperature and pressure for the conversion to complete. Electrochemical CO₂ reduction, in comparison, can be initiated by renewable electricity under ambient conditions. To lower the activation energy barrier of CO₂ and to convert CO₂ to value-added chemicals, active, selective, and stable catalysts need first to be developed. Catalyst-electrolyte interfaces should also be well-engineered to eliminate all interfacial and mass transport issues during the reaction. Despite the great advances made in these areas, the development of efficient catalysts still posts some serious challenges for practical applications.

Integrated CO₂ capture and conversion removes the cost of CO₂ release and compression and could potentially improve the overall energy efficiency of the system. Recently, the feasibility and potential benefits of integrated CO₂ capture and conversion systems have been demonstrated. But still, there is much to do in research and development to uncover the fundamental mechanisms that lead to efficient transformation of the captured CO₂ to the targeted carbon products. Once the new catalysts and the reduction processes are materialized, coupling CO₂ conversion with direct air capture will become a true integrated technology for realizing negative CO₂ emission and energy sustainability.

Conflicts of interest

There are no conflicts of interest to declare.

Acknowledgements

Recent work was supported by the NSF under Grants CHE-2102290 (Brown), CHE-2102245 (the University of Connecticut), and by Brown's Office of Vice President for Research.

References

- 1 T. J. Battin, S. Luysaert, L. A. Kaplan, A. K. Aufdenkampe, A. Richter and L. J. Tranvik, *Nat. Geosci.*, 2009, 2, 598–600.

- 2 R. A. Berner, *Nature*, 2003, **426**, 323–326.
- 3 E. T. Mitchard, *Nature*, 2018, **559**, 527–534.
- 4 E. Eriksson and P. Welander, *Tellus*, 1956, **8**, 154–175.
- 5 J. E. Bauer, W.-J. Cai, P. A. Raymond, T. S. Bianchi, C. S. Hopkinson and P. A. Regnier, *Nature*, 2013, **504**, 61–70.
- 6 W. H. Schlesinger, *Soils and Global Change*, 1995, vol. 25, pp. 9–25.
- 7 P. M. Cox, R. A. Betts, C. D. Jones, S. A. Spall and I. J. Totterdell, *Nature*, 2000, **408**, 184–187.
- 8 M. Reichstein, M. Bahn, P. Ciais, D. Frank, M. D. Mahecha, S. I. Seneviratne, J. Zscheischler, C. Beer, N. Buchmann and D. C. Frank, *Nature*, 2013, **500**, 287–295.
- 9 J. Randers, *2052: A global forecast for the next forty years*, Chelsea Green Publishing, 2012.
- 10 J. C. Zachos, G. R. Dickens and R. E. Zeebe, *Nature*, 2008, **451**, 279–283.
- 11 M. Anwar, A. Fayyaz, N. Sohail, M. Khokhar, M. Baqar, W. Khan, K. Rasool, M. Rehan and A. Nizami, *J. Environ. Manage.*, 2018, **226**, 131–144.
- 12 B. Li, Y. Duan, D. Luebke and B. Morreale, *Appl. Energy*, 2013, **102**, 1439–1447.
- 13 S. Chuhadiya, D. Suthar, S. Patel and M. Dhaka, *Coord. Chem. Rev.*, 2021, **446**, 214115.
- 14 E. S. Sanz-Perez, C. R. Murdock, S. A. Didas and C. W. Jones, *Chem. Rev.*, 2016, **116**, 11840–11876.
- 15 X. Shi, H. Xiao, H. Azarabadi, J. Song, X. Wu, X. Chen and K. S. Lackner, *Angew. Chem., Int. Ed.*, 2020, **59**, 6984–7006.
- 16 C. R. Murdock, S. Didas and C. W. Jones, *Chem. Rev.*, 2016, **116**(19), 11840–11876.
- 17 G. Singh, J. Lee, A. Karakoti, R. Bahadur, J. Yi, D. Zhao, K. AlBahily and A. Vinu, *Chem. Soc. Rev.*, 2020, **49**, 4360–4404.
- 18 S. Zeng, X. Zhang, L. Bai, X. Zhang, H. Wang, J. Wang, D. Bao, M. Li, X. Liu and S. Zhang, *Chem. Rev.*, 2017, **117**, 9625–9673.
- 19 G. Kupgan, L. J. Abbott, K. E. Hart and C. M. Colina, *Chem. Rev.*, 2018, **118**, 5488–5538.
- 20 J. K. Stolaroff, D. W. Keith and G. V. Lowry, *Environ. Sci. Technol.*, 2008, **42**, 2728–2735.
- 21 M. T. Dunstan, F. Donat, A. H. Bork, C. P. Grey and C. R. Müller, *Chem. Rev.*, 2021, **121**, 12681–12745.
- 22 X. Yang, R. J. Rees, W. Conway, G. Puxty, Q. Yang and D. A. Winkler, *Chem. Rev.*, 2017, **117**, 9524–9593.
- 23 A. Goeppert, M. Czaun, G. S. Prakash and G. A. Olah, *Energy Environ. Sci.*, 2012, **5**, 7833–7853.
- 24 P. Bollini, S. A. Didas and C. W. Jones, *J. Mater. Chem.*, 2011, **21**, 15100–15120.
- 25 W. Li, S. Choi, J. H. Drese, M. Hornbostel, G. Krishnan, P. M. Eisenberger and C. W. Jones, *ChemSusChem*, 2010, **3**, 899–903.
- 26 S. A. Didas, *Structural properties of aminosilica materials for CO₂ capture*, Georgia Institute of Technology, 2014.
- 27 N. R. Stuckert and R. T. Yang, *Environ. Sci. Technol.*, 2011, **45**, 10257–10264.
- 28 O. K. Farha, I. Eryazici, N. C. Jeong, B. G. Hauser, C. E. Wilmer, A. A. Sarjeant, R. Q. Snurr, S. T. Nguyen, A. O. z. r. Yazaydin and J. T. Hupp, *J. Am. Chem. Soc.*, 2012, **134**, 15016–15021.
- 29 Y. Z. Li, H. H. Wang, H. Y. Yang, L. Hou, Y. Y. Wang and Z. Zhu, *Chem. – Eur. J.*, 2018, **24**, 865–871.
- 30 A. Modak and S. Jana, *Microporous Mesoporous Mater.*, 2019, **276**, 107–132.
- 31 A. O. Yazaydin, A. I. Benin, S. A. Faheem, P. Jakubczak, J. J. Low, R. R. Willis and R. Q. Snurr, *Chem. Mater.*, 2009, **21**, 1425–1430.
- 32 D.-A. Yang, H.-Y. Cho, J. Kim, S.-T. Yang and W.-S. Ahn, *Energy Environ. Sci.*, 2012, **5**, 6465–6473.
- 33 X. Kong, E. Scott, W. Ding, J. A. Mason, J. R. Long and J. A. Reimer, *J. Am. Chem. Soc.*, 2012, **134**, 14341–14344.
- 34 R. Poloni, K. Lee, R. F. Berger, B. Smit and J. B. Neaton, *J. Phys. Chem. Lett.*, 2014, **5**, 861–865.
- 35 H. Li, K. Wang, Z. Hu, Y.-P. Chen, W. Verdegaal, D. Zhao and H.-C. Zhou, *J. Mater. Chem. A*, 2019, **7**, 7867–7874.
- 36 A. M. Fracaroli, H. Furukawa, M. Suzuki, M. Dodd, S. Okajima, F. Gándara, J. A. Reimer and O. M. Yaghi, *J. Am. Chem. Soc.*, 2014, **136**, 8863–8866.
- 37 R. W. Flaig, T. M. Osborn Popp, A. M. Fracaroli, E. A. Kapustin, M. J. Kalmutzki, R. M. Altamimi, F. Fathieh, J. A. Reimer and O. M. Yaghi, *J. Am. Chem. Soc.*, 2017, **139**, 12125–12128.
- 38 S.-J. Bao, R. Krishna, Y.-B. He, J.-S. Qin, Z.-M. Su, S.-L. Li, W. Xie, D.-Y. Du, W.-W. He and S.-R. Zhang, *J. Mater. Chem. A*, 2015, **3**, 7361–7367.
- 39 Z. Hu, Y. Wang, S. Farooq and D. Zhao, *AIChE J.*, 2017, **63**, 4103–4114.
- 40 W. Meng, Y. Zeng, Z. Liang, W. Guo, C. Zhi, Y. Wu, R. Zhong, C. Qu and R. Zou, *ChemSusChem*, 2018, **11**, 3751–3757.
- 41 B. L. Suh, S. Lee and J. Kim, *J. Phys. Chem. C*, 2017, **121**, 24444–24451.
- 42 S. Nakamura, M. Hatakeyama, Y. Wang, K. Ogata and K. Fujii, in *Advances in CO₂ Capture, Sequestration, and Conversion*, ACS Publications, 2015, pp. 123–134.
- 43 J. M. Weber, *Int. Rev. Phys. Chem.*, 2014, **33**, 489–519.
- 44 L. G. Dodson, M. C. Thompson and J. M. Weber, *Annu. Rev. Phys. Chem.*, 2018, **69**, 231–252.
- 45 B. J. Knurr and J. M. Weber, *J. Phys. Chem. A*, 2014, **118**, 4056–4062.
- 46 B. J. Knurr and J. M. Weber, *J. Phys. Chem. A*, 2014, **118**, 8753–8757.
- 47 M. C. Thompson, L. G. Dodson and J. M. Weber, *J. Phys. Chem. A*, 2017, **121**, 4132–4138.
- 48 B. M. Tackett, E. Gomez and J. G. Chen, *Nat. Catal.*, 2019, **2**, 381–386.
- 49 C. Song, *Catal. Today*, 2006, **115**, 2–32.
- 50 W. Li, H. Wang, X. Jiang, J. Zhu, Z. Liu, X. Guo and C. Song, *RSC Adv.*, 2018, **8**, 7651–7669.
- 51 Y. A. Daza and J. N. Kuhn, *RSC Adv.*, 2016, **6**, 49675–49691.
- 52 T. Riedel, G. Schaub, K.-W. Jun and K.-W. Lee, *Ind. Eng. Chem. Res.*, 2001, **40**, 1355–1363.

- 53 M. J. L. Ginés, A. J. Marchi and C. R. Apesteguía, *Appl. Catal., A*, 1997, **154**, 155–171.
- 54 S.-I. Fujita, M. Usui and N. Takezawa, *J. Catal.*, 1992, **134**, 220–225.
- 55 C.-S. Chen, W.-H. Cheng and S.-S. Lin, *Catal. Lett.*, 2000, **68**, 45–48.
- 56 M. D. Porosoff, B. Yan and J. G. Chen, *Energy Environ. Sci.*, 2016, **9**, 62–73.
- 57 S. Kattel, P. Liu and J. G. Chen, *J. Am. Chem. Soc.*, 2017, **139**, 9739–9754.
- 58 M. D. Porosoff and J. G. Chen, *J. Catal.*, 2013, **301**, 30–37.
- 59 J. C. Matsubu, V. N. Yang and P. Christopher, *J. Am. Chem. Soc.*, 2015, **137**, 3076–3084.
- 60 X. Zhang, X. Zhu, L. Lin, S. Yao, M. Zhang, X. Liu, X. Wang, Y.-W. Li, C. Shi and D. Ma, *ACS Catal.*, 2017, **7**, 912–918.
- 61 S.-C. Yang, S. H. Pang, T. P. Sulmonetti, W.-N. Su, J.-F. Lee, B.-J. Hwang and C. W. Jones, *ACS Catal.*, 2018, **8**, 12056–12066.
- 62 X. Jiang, X. Nie, X. Guo, C. Song and J. G. Chen, *Chem. Rev.*, 2020, **120**, 7984–8034.
- 63 G. A. Olah, A. Goeppert and G. K. S. Prakash, in *Beyond Oil and Gas: The Methanol Economy*, Wiley-VCH, Weinheim, 2009, pp. 179–184.
- 64 S.-T. Bai, G. De Smet, Y. Liao, R. Sun, C. Zhou, M. Beller, B. U. W. Maes and B. F. Sels, *Chem. Soc. Rev.*, 2021, **50**, 4259–4298.
- 65 J. S. Lee, K. H. Lee, S. Y. Lee and Y. G. Kim, *J. Catal.*, 1993, **144**, 414–424.
- 66 S. Kattel, P. J. Ramirez, J. G. Chen, J. A. Rodriguez and P. Liu, *Science*, 2017, **355**, 1296–1299.
- 67 M. Behrens, F. Studt, I. Kasatkin, S. Kühl, M. Hävecker, F. Abild-Pedersen, S. Zander, F. Girgsdies, P. Kurr, B.-L. Knief, M. Tovar, R. W. Fischer, J. K. Nørskov and R. Schlögl, *Science*, 2012, **336**, 893–897.
- 68 E. L. Kunkes, F. Studt, F. Abild-Pedersen, R. Schlögl and M. Behrens, *J. Catal.*, 2015, **328**, 43–48.
- 69 S. Tada, S. Kayamori, T. Honma, H. Kamei, A. Nariyuki, K. Kon, T. Toyao, K.-I. Shimizu and S. Satokawa, *ACS Catal.*, 2018, **8**, 7809–7819.
- 70 B. Rungtaweeworant, J. Baek, J. R. Araujo, B. S. Archanjo, K. M. Choi, O. M. Yaghi and G. A. Somorjai, *Nano Lett.*, 2016, **16**, 7645–7649.
- 71 F. Studt, I. Sharafutdinov, F. Abild-Pedersen, C. F. Elkjær, J. S. Hummelshøj, S. Dahl, I. Chorkendorff and J. K. Nørskov, *Nat. Chem.*, 2014, **6**, 320–324.
- 72 A. García-Trenco, A. Regoutz, E. R. White, D. J. Payne, M. S. P. Shaffer and C. K. Williams, *Appl. Catal., B*, 2018, **220**, 9–18.
- 73 O. Martin, A. J. Martín, C. Mondelli, S. Mitchell, T. F. Segawa, R. Hauert, C. Drouilly, D. Curulla-Ferré and J. Pérez-Ramírez, *Angew. Chem., Int. Ed.*, 2016, **55**, 6261–6265.
- 74 E. C. Ra, K. Y. Kim, E. H. Kim, H. Lee, K. An and J. S. Lee, *ACS Catal.*, 2020, **10**, 11318–11345.
- 75 I. Amghizar, L. A. Vandewalle, K. M. Van Geem and G. B. Marin, *Engineering*, 2017, **3**, 171–178.
- 76 W. Zhou, K. Cheng, J. Kang, C. Zhou, V. Subramanian, Q. Zhang and Y. Wang, *Chem. Soc. Rev.*, 2019, **48**, 3193–3228.
- 77 R.-P. Ye, J. Ding, W. Gong, M. D. Argyle, Q. Zhong, Y. Wang, C. K. Russell, Z. Xu, A. G. Russell, Q. Li, M. Fan and Y.-G. Yao, *Nat. Commun.*, 2019, **10**, 5698.
- 78 J. Chai, R. Pestman, W. Chen, N. Donkervoet, A. I. Dugulan, Z. Men, P. Wang and E. J. Hensen, *ACS Catal.*, 2022, **12**, 2877–2887.
- 79 Q.-Y. Liu, C. Shang and Z.-P. Liu, *J. Phys. Chem. Lett.*, 2022, **13**, 3342–3352.
- 80 A. E. Rashed, A. Nasser, M. F. Elkady, Y. Matsushita and A. A. El-Moneim, *ACS Omega*, 2022, **7**, 8403–8419.
- 81 R. W. Dorner, D. R. Hardy, F. W. Williams and H. D. Willauer, *Energy Environ. Sci.*, 2010, **3**, 884–890.
- 82 J. Wei, J. Sun, Z. Wen, C. Fang, Q. Ge and H. Xu, *Catal. Sci. Technol.*, 2016, **6**, 4786–4793.
- 83 A. Ramirez, L. Gevers, A. Bavykina, S. Ould-Chikh and J. Gascon, *ACS Catal.*, 2018, **8**, 9174–9182.
- 84 W. Wang, X. Jiang, X. Wang and C. Song, *Ind. Eng. Chem. Res.*, 2018, **57**, 4535–4542.
- 85 R. Sathawong, N. Koizumi, C. Song and P. Prasassarakich, *J. CO₂ Util.*, 2013, **3–4**, 102–106.
- 86 J. Wang, Z. You, Q. Zhang, W. Deng and Y. Wang, *Catal. Today*, 2013, **215**, 186–193.
- 87 S. Gupta, V. K. Jain and D. Jagadeesan, *ChemNanoMat*, 2016, **2**, 989–996.
- 88 D. Wang, Z. Xie, M. D. Porosoff and J. G. Chen, *Chem*, 2021, **7**, 2277–2311.
- 89 K. B. Tan, G. Zhan, D. Sun, J. Huang and Q. Li, *J. Mater. Chem. A*, 2021, **9**, 5197–5231.
- 90 L. Fan, C. Xia, F. Yang, J. Wang, H. Wang and Y. Lu, *Sci. Adv.*, 2020, **6**, eaay3111.
- 91 Z. Sun, Y. Hu, D. Zhou, M. Sun, S. Wang and W. Chen, *ACS Energy Lett.*, 2021, **6**, 3992–4022.
- 92 T. K. Todorova, M. W. Schreiber and M. Fontecave, *ACS Catal.*, 2019, **10**, 1754–1768.
- 93 Z. Yin, G. T. R. Palmore and S. Sun, *Trends Chem.*, 2019, **1**, 739–750.
- 94 D. Johnson, Z. Qiao and A. Djire, *ACS Appl. Energy Mater.*, 2021, **4**, 8661–8684.
- 95 S. Nitopi, E. Bertheussen, S. B. Scott, X. Liu, A. K. Engstfeld, S. Horch, B. Seger, I. E. Stephens, K. Chan and C. Hahn, *Chem. Rev.*, 2019, **119**, 7610–7672.
- 96 H. Zhang, Y. Zhang, Y. Li, S. Ahn, G. T. R. Palmore, J. Fu, A. A. Peterson and S. Sun, *Nanoscale*, 2019, **11**, 12075–12079.
- 97 J. Fu, W. Zhu, Y. Chen, Z. Yin, Y. Li, J. Liu, H. Zhang, J. J. Zhu and S. Sun, *Angew. Chem.*, 2019, **131**, 14238–14241.
- 98 W. Zhu, R. Michalsky, O. N. Metin, H. Lv, S. Guo, C. J. Wright, X. Sun, A. A. Peterson and S. Sun, *J. Am. Chem. Soc.*, 2013, **135**, 16833–16836.
- 99 W. Zhu, Y.-J. Zhang, H. Zhang, H. Lv, Q. Li, R. Michalsky, A. A. Peterson and S. Sun, *J. Am. Chem. Soc.*, 2014, **136**, 16132–16135.

- 100 D. Gao, H. Zhou, J. Wang, S. Miao, F. Yang, G. Wang, J. Wang and X. Bao, *J. Am. Chem. Soc.*, 2015, **137**, 4288–4291.
- 101 C. Kim, H. S. Jeon, T. Eom, M. S. Jee, H. Kim, C. M. Friend, B. K. Min and Y. J. Hwang, *J. Am. Chem. Soc.*, 2015, **137**, 13844–13850.
- 102 Q. Li, J. Fu, W. Zhu, Z. Chen, B. Shen, L. Wu, Z. Xi, T. Wang, G. Lu and J.-J. Zhu, *J. Am. Chem. Soc.*, 2017, **139**, 4290–4293.
- 103 P. Hou, X. Wang, Z. Wang and P. Kang, *ACS Appl. Mater. Interfaces*, 2018, **10**, 38024–38031.
- 104 S. Zhang, P. Kang and T. J. Meyer, *J. Am. Chem. Soc.*, 2014, **136**, 1734–1737.
- 105 D. Gao, H. Zhou, F. Cai, J. Wang, G. Wang and X. Bao, *ACS Catal.*, 2018, **8**, 1510–1519.
- 106 C. W. Lee, J. S. Hong, K. D. Yang, K. Jin, J. H. Lee, H.-Y. Ahn, H. Seo, N.-E. Sung and K. T. Nam, *ACS Catal.*, 2018, **8**, 931–937.
- 107 X. Sun, L. Lu, Q. Zhu, C. Wu, D. Yang, C. Chen and B. Han, *Angew. Chem., Int. Ed.*, 2018, **57**, 2427–2431.
- 108 Q. Zhu, X. Sun, D. Yang, J. Ma, X. Kang, L. Zheng, J. Zhang, Z. Wu and B. Han, *Nat. Commun.*, 2019, **10**, 1–11.
- 109 C. W. Li and M. W. Kanan, *J. Am. Chem. Soc.*, 2012, **134**, 7231–7234.
- 110 Y. Zhao, X. Zu, R. Chen, X. Li, Y. Jiang, Z. Wang, S. Wang, Y. Wu, Y. Sun and Y. Xie, *J. Am. Chem. Soc.*, 2022, **144**, 10446–10454.
- 111 S. Mu, H. Lu, Q. Wu, L. Li, R. Zhao, C. Long and C. Cui, *Nat. Commun.*, 2022, **13**, 1–8.
- 112 X. Wang, K. Klingan, M. Klingenhof, T. Möller, J. Ferreira de Araújo, I. Martens, A. Bagger, S. Jiang, J. Rossmeisl and H. Dau, *Nat. Commun.*, 2021, **12**, 1–12.
- 113 S. H. Lee, J. C. Lin, M. Farmand, A. T. Landers, J. T. Feaster, J. E. Avilés Acosta, J. W. Beeman, Y. Ye, J. Yano and A. Mehta, *J. Am. Chem. Soc.*, 2020, **143**, 588–592.
- 114 S.-C. Lin, C.-C. Chang, S.-Y. Chiu, H.-T. Pai, T.-Y. Liao, C.-S. Hsu, W.-H. Chiang, M.-K. Tsai and H. M. Chen, *Nat. Commun.*, 2020, **11**, 1–12.
- 115 Z. Yin, C. Yu, Z. Zhao, X. Guo, M. Shen, N. Li, M. Muzzio, J. Li, H. Liu and H. Lin, *Nano Lett.*, 2019, **19**, 8658–8663.
- 116 S. Meshitsuka, M. Ichikawa and K. Tamaru, *J. Chem. Soc., Chem. Commun.*, 1974, 158–159.
- 117 M. Li, H. Wang, W. Luo, P. C. Sherrell, J. Chen and J. Yang, *Adv. Mater.*, 2020, **32**, 2001848.
- 118 J. Yang, Z. Qiu, C. Zhao, W. Wei, W. Chen, Z. Li, Y. Qu, J. Dong, J. Luo and Z. Li, *Angew. Chem., Int. Ed.*, 2018, **57**, 14095–14100.
- 119 X. Wang, Z. Chen, X. Zhao, T. Yao, W. Chen, R. You, C. Zhao, G. Wu, J. Wang and W. Huang, *Angew. Chem.*, 2018, **130**, 1962–1966.
- 120 Q. Qu, S. Ji, Y. Chen, D. Wang and Y. Li, *Chem. Sci.*, 2021, **12**, 4201–4215.
- 121 Y. Wang, H. Su, Y. He, L. Li, S. Zhu, H. Shen, P. Xie, X. Fu, G. Zhou and C. Feng, *Chem. Rev.*, 2020, **120**, 12217–12314.
- 122 C. Shi, H. A. Hansen, A. C. Lausche and J. K. Nørskov, *Phys. Chem. Chem. Phys.*, 2014, **16**, 4720–4727.
- 123 Y. Hori, H. Wakebe, T. Tsukamoto and O. Koga, *Electrochim. Acta*, 1994, **39**, 1833–1839.
- 124 A. Bagger, W. Ju, A. S. Varela, P. Strasser and J. Rossmeisl, *ChemPhysChem*, 2017, **18**, 3266–3273.
- 125 C. W. Lee, K. D. Yang, D. H. Nam, J. H. Jang, N. H. Cho, S. W. Im and K. T. Nam, *Adv. Mater.*, 2018, **30**, 1704717.
- 126 H. Yano, F. Shirai, M. Nakayama and K. Ogura, *J. Electroanal. Chem.*, 2002, **533**, 113–118.
- 127 T. Burdyny, P. J. Graham, Y. Pang, C.-T. Dinh, M. Liu, E. H. Sargent and D. Sinton, *ACS Sustainable Chem. Eng.*, 2017, **5**, 4031–4040.
- 128 K. Junge Puring, D. Siegmund, J. Timm, F. Möllenbruck, S. Schemme, R. Marschall and U. P. Apfel, *Adv. Sustainable Syst.*, 2021, **5**, 2000088.
- 129 Z. Zhan and L. Zhao, *J. Power Sources*, 2010, **195**, 7250–7254.
- 130 M. Moura de Salles Pupo and R. Kortlever, *ChemPhysChem*, 2019, **20**, 2926–2935.
- 131 J.-B. Vennekötter, T. Scheuermann, R. Sengpiel and M. Wessling, *J. CO₂ Util.*, 2019, **32**, 202–213.
- 132 S. Lu, Y. Wang, H. Xiang, H. Lei, B. B. Xu, L. Xing, E. H. Yu and T. X. Liu, *J. Energy Storage*, 2022, **52**, 104764.
- 133 D. T. Hofsommer, Y. Liang, S. S. Uttarwar, M. Gautam, S. Pishgar, S. Gulati, C. A. Grapperhaus and J. M. Spurgeon, *ChemSusChem*, 2022, **15**, e202102289.
- 134 S. Zhang, P. Kang, S. Ubnoske, M. K. Brennaman, N. Song, R. L. House, J. T. Glass and T. J. Meyer, *J. Am. Chem. Soc.*, 2014, **136**, 7845–7848.
- 135 M. S. Xie, B. Y. Xia, Y. Li, Y. Yan, Y. Yang, Q. Sun, S. H. Chan, A. Fisher and X. Wang, *Energy Environ. Sci.*, 2016, **9**, 1687–1695.
- 136 Y. Qiu, H. Zhong, W. Xu, T. Zhang, X. Li and H. Zhang, *J. Mater. Chem. A*, 2019, **7**, 5453–5462.
- 137 L. Jin, B. Liu, P. Wang, H. Yao, L. A. Achola, P. Kerns, A. Lopes, Y. Yang, J. Ho and A. Moewes, *Nanoscale*, 2018, **10**, 14678–14686.
- 138 L. Jin, E. Shaaban, S. Bamonte, D. Cintron, S. Shuster, L. Zhang, G. Li and J. He, *ACS Appl. Mater. Interfaces*, 2021, **13**, 38595–38603.
- 139 X. Su, Y. Sun, L. Jin, L. Zhang, Y. Yang, P. Kerns, B. Liu, S. Li and J. He, *Appl. Catal., B*, 2020, **269**, 118800.
- 140 J. C. Bui, C. Kim, A. J. King, O. Romiluyi, A. Kusoglu, A. Z. Weber and A. T. Bell, *Acc. Chem. Res.*, 2022, **55**, 484–494.
- 141 Q. Fan, M. Zhang, M. Jia, S. Liu, J. Qiu and Z. Sun, *Mater. Today Energy*, 2018, **10**, 280–301.
- 142 L. Fan, C.-Y. Liu, P. Zhu, C. Xia, X. Zhang, Z.-Y. Wu, Y. Lu, T. P. Senftle and H. Wang, *Joule*, 2022, **6**, 205–220.
- 143 Y. J. Sa, C. W. Lee, S. Y. Lee, J. Na, U. Lee and Y. J. Hwang, *Chem. Soc. Rev.*, 2020, **49**, 6632–6665.
- 144 H. Hashiba, L.-C. Weng, Y. Chen, H. K. Sato, S. Yotsuhashi, C. Xiang and A. Z. Weber, *J. Phys. Chem. C*, 2018, **122**, 3719–3726.

- 145 R. Casebolt, K. W. Kimura, K. Levine, J. A. Cimada DaSilva, J. Kim, T. A. Dunbar, J. Suntivich and T. Hanrath, *ChemElectroChem*, 2021, **8**, 681–688.
- 146 A. S. Varela, M. Kroschel, T. Reier and P. Strasser, *Catal. Today*, 2016, **260**, 8–13.
- 147 M. R. Singh, E. L. Clark and A. T. Bell, *Phys. Chem. Chem. Phys.*, 2015, **17**, 18924–18936.
- 148 C. Kim, J. C. Bui, X. Luo, J. K. Cooper, A. Kusoglu, A. Z. Weber and A. T. Bell, *Nat. Energy*, 2021, **6**, 1026–1034.
- 149 M. T. Koper, *Chem. Sci.*, 2013, **4**, 2710–2723.
- 150 X. Lu, C. Zhu, Z. Wu, J. Xuan, J. S. Francisco and H. Wang, *J. Am. Chem. Soc.*, 2020, **142**, 15438–15444.
- 151 M. König, J. Vaes, E. Klemm and D. Pant, *iScience*, 2019, **19**, 135–160.
- 152 J. Li, Y. Kuang, Y. Meng, X. Tian, W.-H. Hung, X. Zhang, A. Li, M. Xu, W. Zhou, C.-S. Ku, C.-Y. Chiang, G. Zhu, J. Guo, X. Sun and H. Dai, *J. Am. Chem. Soc.*, 2020, **142**, 7276–7282.
- 153 A. S. Hall, Y. Yoon, A. Wuttig and Y. Surendranath, *J. Am. Chem. Soc.*, 2015, **137**, 14834–14837.
- 154 Y. Zou and S. Wang, *Adv. Sci.*, 2021, **8**, 2003579.
- 155 R. Kas, R. Kortlever, H. Yilmaz, M. T. M. Koper and G. Mul, *ChemElectroChem*, 2015, **2**, 354–358.
- 156 M. R. Singh, Y. Kwon, Y. Lum, J. W. Ager and A. T. Bell, *J. Am. Chem. Soc.*, 2016, **138**, 13006–13012.
- 157 J. Resasco, L. D. Chen, E. Clark, C. Tsai, C. Hahn, T. F. Jaramillo, K. Chan and A. T. Bell, *J. Am. Chem. Soc.*, 2017, **139**, 11277–11287.
- 158 D. Gao, F. Scholten and B. Roldan Cuenya, *ACS Catal.*, 2017, **7**, 5112–5120.
- 159 J. Resasco, Y. Lum, E. Clark, J. Z. Zeledon and A. T. Bell, *ChemElectroChem*, 2018, **5**, 1064–1072.
- 160 Y. Ma, J. Wang, J. Yu, J. Zhou, X. Zhou, H. Li, Z. He, H. Long, Y. Wang and P. Lu, *Matter*, 2021, **4**, 888–926.
- 161 F. Li, A. Thevenon, A. Rosas-Hernández, Z. Wang, Y. Li, C. M. Gabardo, A. Ozden, C. T. Dinh, J. Li and Y. Wang, *Nature*, 2020, **577**, 509–513.
- 162 L. Zhang, Z. Wei, S. Thanneeru, M. Meng, M. Kruzyk, G. Ung, B. Liu and J. He, *Angew. Chem.*, 2019, **131**, 15981–15987.
- 163 Y. Wu, Z. Jiang, X. Lu, Y. Liang and H. Wang, *Nature*, 2019, **575**, 639–642.
- 164 Z. Cao, D. Kim, D. Hong, Y. Yu, J. Xu, S. Lin, X. Wen, E. M. Nichols, K. Jeong, J. A. Reimer, P. Yang and C. J. Chang, *J. Am. Chem. Soc.*, 2016, **138**, 8120–8125.
- 165 K. Jiang, Y. Huang, G. Zeng, F. M. Toma, W. A. Goddard III and A. T. Bell, *ACS Energy Lett.*, 2020, **5**, 1206–1214.
- 166 H. Mistry, Y. W. Choi, A. Bagger, F. Scholten, C. S. Bonifacio, I. Sinev, N. J. Divins, I. Zegkinoglou, H. S. Jeon and K. Kisslinger, *Angew. Chem.*, 2017, **129**, 11552–11556.
- 167 Q. Zhu, C. J. Murphy and L. R. Baker, *J. Am. Chem. Soc.*, 2022, **144**, 2829–2840.
- 168 D. Wakerley, S. Lamaison, F. Ozanam, N. Menguy, D. Mercier, P. Marcus, M. Fontecave and V. Mougél, *Nat. Mater.*, 2019, **18**, 1222–1227.
- 169 D. Kim, S. Yu, F. Zheng, I. Roh, Y. Li, S. Louisia, Z. Qi, G. A. Somorjai, H. Frei and L.-W. Wang, *Nat. Energy*, 2020, **5**, 1032–1042.
- 170 S. Yu, S. Louisia and P. Yang, *JACS Au*, 2022, **2**, 562–572.
- 171 J. Tamura, A. Ono, Y. Sugano, C. Huang, H. Nishizawa and S. Mikoshiba, *Phys. Chem. Chem. Phys.*, 2015, **17**, 26072–26078.
- 172 Y. Wang, H. Su, C. Xu, G. Li, L. Gell, S. Lin, Z. Tang, H. Häkkinen and N. Zheng, *J. Am. Chem. Soc.*, 2015, **137**, 4324–4327.
- 173 H. Shang, S. K. Wallentine, D. M. Hofmann, Q. Zhu, C. J. Murphy and L. R. Baker, *Chem. Sci.*, 2020, **11**, 12298–12306.
- 174 F. Pan and Y. Yang, *Energy Environ. Sci.*, 2020, **13**, 2275–2309.
- 175 Y. Fang and J. C. Flake, *J. Am. Chem. Soc.*, 2017, **139**, 3399–3405.
- 176 E. Barton Cole, P. S. Lakkaraju, D. M. Rampulla, A. J. Morris, E. Abelev and A. B. Bocarsly, *J. Am. Chem. Soc.*, 2010, **132**, 11539–11551.
- 177 P. De la Presa, M. Multigner, J. De la Venta, M. García and M. Ruiz-González, *J. Appl. Phys.*, 2006, **100**, 123915.
- 178 S. Sun and H. Zeng, *J. Am. Chem. Soc.*, 2002, **124**, 8204–8205.
- 179 R. Hao, R. Xing, Z. Xu, Y. Hou, S. Gao and S. Sun, *Adv. Mater.*, 2010, **22**, 2729–2742.
- 180 V. Mazumder and S. Sun, *J. Am. Chem. Soc.*, 2009, **131**, 4588–4589.
- 181 C. Wang, H. Daimon, T. Onodera, T. Koda and S. Sun, *Angew. Chem.*, 2008, **120**, 3644–3647.
- 182 Y. Zhao, C. Wang, Y. Liu, D. R. MacFarlane and G. G. Wallace, *Adv. Energy Mater.*, 2018, **8**, 1801400.
- 183 C. Kim, T. Eom, M. S. Jee, H. Jung, H. Kim, B. K. Min and Y. J. Hwang, *ACS Catal.*, 2017, **7**, 779–785.
- 184 M. R. Narouz, K. M. Osten, P. J. Unsworth, R. W. Y. Man, K. Salorinne, S. Takano, R. Tomihara, S. Kaappa, S. Malola, C.-T. Dinh, J. D. Padmos, K. Ayoo, P. J. Garrett, M. Nambo, J. H. Horton, E. H. Sargent, H. Häkkinen, T. Tsukuda and C. M. Crudden, *Nat. Chem.*, 2019, **11**, 419–425.
- 185 L. Zhang, Z. Wei, M. Meng, G. Ung and J. He, *J. Mater. Chem. A*, 2020, **8**, 15900–15908.
- 186 M. N. Hopkinson, C. Richter, M. Schedler and F. Glorius, *Nature*, 2014, **510**, 485–496.
- 187 T. Dröge and F. Glorius, *Angew. Chem., Int. Ed.*, 2010, **49**, 6940–6952.
- 188 D. J. Nelson and S. P. Nolan, *Chem. Soc. Rev.*, 2013, **42**, 6723–6753.
- 189 S. Engel, E.-C. Fritz and B. J. Ravoo, *Chem. Soc. Rev.*, 2017, **46**, 2057–2075.
- 190 C. M. Crudden, J. H. Horton, M. R. Narouz, Z. Li, C. A. Smith, K. Munro, C. J. Baddeley, C. R. Larrea, B. Drevniok, B. Thanabalasingam, A. B. McLean, O. V. Zenkina, I. I. Ebralidze, Z. She, H.-B. Kraatz,

- N. J. Mosey, L. N. Saunders and A. Yagi, *Nat. Commun.*, 2016, **7**, 12654.
- 191 Z. Cao, J. S. Derrick, J. Xu, R. Gao, M. Gong, E. M. Nichols, P. T. Smith, X. Liu, X. Wen, C. Copéret and C. J. Chang, *Angew. Chem., Int. Ed.*, 2018, **57**, 4981–4985.
- 192 S. Sun, *Nat. Energy*, 2020, **5**, 943–944.
- 193 C. M. Jens, L. Müller, K. Leonhard and A. Bardow, *ACS Sustainable Chem. Eng.*, 2019, **7**, 12270–12280.
- 194 S. Kar, A. Goepfert and G. K. S. Prakash, *Acc. Chem. Res.*, 2019, **52**, 2892–2903.
- 195 I. Sullivan, A. Goryachev, I. A. Digdaya, X. Li, H. A. Atwater, D. A. Vermaas and C. Xiang, *Nat. Catal.*, 2021, **4**, 952–958.
- 196 Y.-N. Li, L.-N. He, A.-H. Liu, X.-D. Lang, Z.-Z. Yang, B. Yu and C.-R. Luan, *Green Chem.*, 2013, **15**, 2825–2829.
- 197 J. Kothandaraman, A. Goepfert, M. Czaun, G. A. Olah and G. K. Surya Prakash, *Green Chem.*, 2016, **18**, 5831–5838.
- 198 J. Kothandaraman, A. Goepfert, M. Czaun, G. A. Olah and G. K. S. Prakash, *J. Am. Chem. Soc.*, 2016, **138**, 778–781.
- 199 R. Sen, A. Goepfert, S. Kar and G. K. S. Prakash, *J. Am. Chem. Soc.*, 2020, **142**, 4544–4549.
- 200 T. Li, E. W. Lees, M. Goldman, D. A. Salvatore, D. M. Weekes and C. P. Berlinguette, *Joule*, 2019, **3**, 1487–1497.
- 201 L. Chen, F. Li, Y. Zhang, C. L. Bentley, M. Horne, A. M. Bond and J. Zhang, *ChemSusChem*, 2017, **10**, 4109–4118.
- 202 G. Lee, Y. C. Li, J.-Y. Kim, T. Peng, D.-H. Nam, A. Sedighian Rasouli, F. Li, M. Luo, A. H. Ip, Y.-C. Joo and E. H. Sargent, *Nat. Energy*, 2021, **6**, 46–53.